Microwave resonator lattices for topological photonics [Invited]

Mattis Reisner, Matthieu Bellec, Ulrich Kuhl, Fabrice Mortessagne

Review Vol. 11, No. 3 / 1 March 2021 / Optical Materials Express 629
Optical Materials EXPRESS

Microwave resonator lattices for topological photonics [Invited]

MATTIS REISNER, MATTHIEU BELLEC, ULRICH KUHL, AND FABRICE MORTESSAGNE*

Université Côte d'Azur, CNRS, Institut de Physique de Nice (INPHYNI), 06108 Nice, EU, France
**fabrice.mortessagne@unice.fr*

Abstract: We present a microwave experimental setup emulating tight-binding systems that is now widely used in the realm of topological photonics. A thorough description of the experimental building blocks is presented, showing the advantages and the limits of this platform. Various experimental realizations are then described, ranging from the selective enhancement of a defect state in a non-Hermitian Su-Schrieffer-Heeger (SSH) chain, to the generation of giant pseudo-magnetic fields in deformed honeycomb lattices. Introducing nonlinear losses, the interplay between nonlinearity and topological protection can be engineered to realize a nonlinearly functionalized topological mode with promising applications in receiver protection.

1. Introduction

Topological phases of matter are characterized by a global property – a topological invariant – which make them insensitive to continuous deformation and disorder. Since 1980 with the discovery of the integer quantum Hall effect [1,2], they have been an extensive research area in condensed matter physics. More particularly, topological insulators have attracted a huge interest [3–5]. These materials are crystals that are insulating in the bulk and perfectly conducting at the edges. They exhibit topologically protected surface modes that are immune to back-scattering induced by impurities or disorder. As for the analogy between genuine crystals and photonic crystals [6], Haldane and Raghu first noticed in 2008 that the concepts behind such a topological protection is not restricted to electrons but can also apply for photonic waves traveling in specifically arranged lattices [7]. Topological photonics began experimentally a year later with the observation of scatter-free propagating edge states in a photonic structure operating in the microwave range [8]. Using alternative approaches, based on artificial gauge field, similar behaviors were reported in the IR and visible optical range [9,10]. Since then, a great variety of phenomena directly inspired by topological insulators were experimentally demonstrated (see Ref. [11] for a recent review). Besides direct analogies, intrinsic photonic properties, like loss, gain, or nonlinearity, can be engineered to create new topological systems and study novel concepts at the interface between topological physics and photonics. For instance, topological lasers [12,13] and topological solitons [14–16] were demonstrated recently. In short, topological photonics aims at exploiting the topological robustness to improve the performances of photonic devices from laser sources to waveguides and sensors.

In this context, microwave setups are a driving force in the experimental studies of topological photonic properties in one (1D) or two-dimensional (2D) systems [11]. Indeed, it is worth noting that microwaves sources, detectors and components are routinely accessible and that typical lattice building block scale is cm. It makes topological systems operating in the microwave range rather easy to implement and to manipulate with high sub-wavelength precision. Additionally, complex fields (amplitude and phase) can be measured precisely by means of a vector network analyzer.

We will start this review paper by a brief description of the two main types of experimental microwave platforms characterized by the polarization of the electromagnetic field, namely TM

#416835 https://doi.org/10.1364/OME.416835
Journal © 2021 Received 7 Dec 2020; revised 22 Jan 2021; accepted 25 Jan 2021; published 3 Feb 2021

Optical Materials EXPRESS

or TE (Section 2). Then we will focus on the microwave resonator lattice developed in our group for topological photonics experiments. We will start in Section 3 by a description of a single TE-polarized dielectric resonator. Then Section 4 will describe how these elementary elements are coupled together to form lattices, going even beyond the usual tight-binding description. Section 5 will present how an internal degree of freedom can be exploited to achieve anisotropic coupling between resonators. We exploit transmission measurements in Section 6 giving access to the sign of wave functions as well as the propagation of a local injection, i.e. to the time domain. The last two chapters will propose an overview of the topological situations we addressed with microwave resonator lattices. Section 7 will be devoted to linear systems with various broken symmetries, while Section 8 will describe studies that combine nonlinear losses and topological protection.

2. Microwave platforms

Most of the microwave experiments, involved in the framework of topological photonics, consist in a cavity made of two parallel metallic plates. The lattice structure is placed in the cavity and arranged along (x, y), see Fig. 1(a). The system presents a cylindrical symmetry, i.e. the system is invariant along the perpendicular z-direction. Thus the z and x, y components can be separated and the system can be considered as 2D.

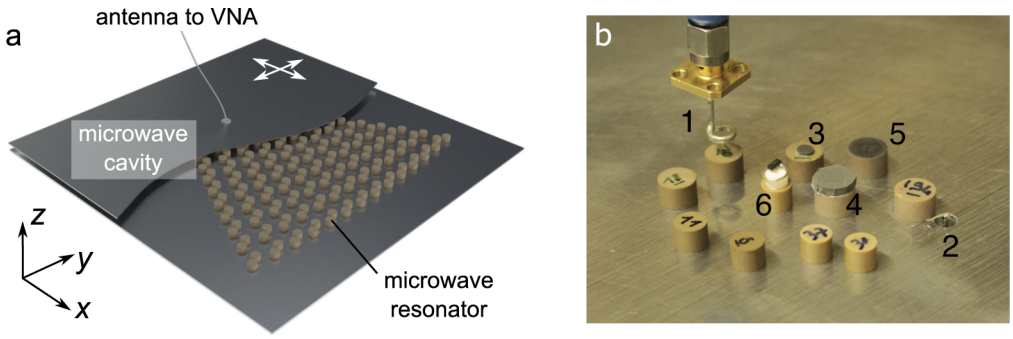

Fig. 1. (a) Typical configuration for microwave topological photonics. A photonic lattice (made of dielectric, metallic, ferritic, or gyro-magnetic materials) is inserted in a microwave cavity made of two metallic plates. Antennas can excite and collect the microwave signal via a vector network analyzer including phase and amplitude information. They can be mobile to spatially resolve the electromagnetic field in the cavity along the (x, y) plane. (b) Typical microwave components used in the setup discussed in this review. The dielectric cylindrical resonators have the same height (5 mm) but their diameter range from 6 to 8 mm. Different kind of antennas (loop, 1 and dipole, 2) allow to excite the TE polarization. On-site losses can be controlled via absorbing patches (3, 4) or sprayed graphite (5) placed on top of the resonators. Nonlinear losses are added via a Schottky diode short-circuited by a metallic loop and placed on a Teflon spacer (6).

One possibility is to use the transverse magnetic mode in z-direction, where the electric field $\vec{E}$ has solely a z-component E_z and does not depend on z (we name it TM_0 mode). Below a cutoff frequency defined by the distance between the two metallic plates, this is the only existing mode and the vectorial nature of the electromagnetic waves can be reduced to a scalar description. In microwave systems composed of passive dielectric or metallic structures, such configurations allow to address Dirac physics in graphene-like photonic crystals [17,18]. Note that beside topological photonics, a plethora of effects were also reported ranging from quantum chaos [19–22] to Anderson localization [23,24]. The full range of symmetries (chiral, time reversal, parity-time ($\mathcal{PT}$), charge-parity ($\mathcal{CP}$)) and their broken versions become accessible introducing

Optical Materials EXPRESS

gyro-magnetic scatterers. Numerous works have been performed ranging from the pioneering observation of unidirectional back-scattering immune states [8] to the realization of quantum (spin) Hall waveguides [25] and the study of disorder-induced topological phase transition [26]. Moreover, emerging applications of microwave topological systems have been recently discussed in [27].

The second typical setup, which we will solely concentrate on in this review, uses the first transverse electric mode (TE_1) in the z-direction. The microwave cavity in which the dielectric resonators have been placed supports resonances in air below the cutoff frequency of this TE_1 mode. Consequently, the resonators are evanescently coupled and realize a tight-binding Hamiltonian system as detailed in Ref. [28] and in Section 4. First graphene-like lattices have been investigated [29], followed by experimental realization of various systems ranging from Dirac oscillator [30] to transport in molecules [31] and nanoribbons [32] to experimental implementation of quantum search algorithms [33] and to give a physical interpretation of the gap labelling in a Penrose tiling [34]. These experiments have been complemented by research on non-Hermitian topological structures in 1D (Su-Schrieffer-Heeger (SSH) chain [35]) and 2D (Lieb lattice [36]). The SSH version was also exploited to implement photonic limiters [37,38]. Topological phase transition [39], edge state manipulation [40] and pseudo-magnetic Landau levels [41] have been also reported in strained honeycomb lattices.

The experimental platform presented in this review consists of cylindrical dielectric Mie resonators [42,43] made of ZrSnTiO ceramics (from Exxelia Temex manufacturer) with a refraction index of $n \approx 6$ embedded in a microwave cavity (see Fig. 1). Within the frequency range we are working, 6 GHz to 9 GHz, and the used height of $h = 10$ mm to 16 mm between the metallic plates, the wave number inside the resonators is real, but outside it is purely imaginary, leading to evanescent fields, and therefore to an evanescent coupling between the resonators, that itself depends on the distance between the resonators [44]. The resonators can be positioned anywhere on a plane with a precision of 0.1 mm using a motorized XY-stage (Newport IMS600CC). For the excitation we use different types of antennas, that ideally excite only TE modes in the cavity: A kink antenna, whose perpendicular part couples to the electrical field parallel to the plane of the cavity, and a loop antenna, which couples to the z-component of the magnetic field, is attached to the top-plate and can be moved in the (x-y) plane above the resonators.

From the amplitude and phase of the reflection signal S_{11} measured by a vector network analyzer (ZVA 24 from Rohde & Schwarz) over a given frequency range, we have direct access to the local density of states (LDOS)

$$\rho(\mathbf{r}_1, \nu) \propto \frac{|S_{11}(\nu)|^2}{\langle |S_{11}|^2 \rangle_\nu} \varphi'_{11}(\nu), \tag{1}$$

where $\langle \ldots \rangle_\nu$ indicates an average over the whole accessible frequency spectrum, $\varphi_{11} = \mathrm{Arg}(S_{11})$ is the phase of the reflected signal, and φ'_{11} denotes its derivative with respect to the frequency ν (see appendix A of Ref. [28]). The density of states (DOS) is obtained by averaging over all positions $\mathbf{r}_1$. Moreover, our setup allows us to visualize the wavefunction associated with each eigenfrequency. According to the definition of the local density of states $\rho(\mathbf{r}_1, \nu) = \sum_n |\Psi_n(\mathbf{r}_1)|^2 \delta(\nu - \nu_n)$, the resonance curve exhibits a maximum whose value is related to the intensity of the wavefunction at the specific position $\mathbf{r}_1$. The intensity distribution for the wavefunction associated with each individual eigenfrequency thus becomes directly accessible [28].

3. Unit cell–electromagnetic description of a single resonator

Considering for now only a single cylindrical resonator with diameter D perfectly sandwiched between two parallel metallic plates, that are separated by a distance h so that there is perfect contact on top and bottom between the resonator and the metallic surface. We can thus separate

Optical Materials EXPRESS

the coordinate along the direction perpendicular to the two plates, say the z-direction, and solve the Helmholtz equation for cylindrical coordinates (r, θ, z) [37]. We concentrate on TE modes, where the wavefunction $\Psi_0(x, y)$ corresponds to the z-component of the magnetic field. Taking into account the continuity-condition for the fields at the resonator-air interface, the lowest TE-mode with harmonic time dependency at frequency ν_0 takes the form [28,37,44,45]

$$\vec{B}(r,z) = (0,0,B_z) = B_0'\Psi_0(r)\sin\frac{\pi z}{h}\vec{e}_z = B_0\sin\frac{\pi z}{h}\cdot\begin{cases} J_0(k_\perp r)\vec{e}_z \text{ for } r<D \\ \alpha\cdot K_0(\gamma r)\vec{e}_z \text{ for } r>D \end{cases}, \tag{2}$$

where J_0 and K_0 are Bessel functions with the wave numbers $k_\perp = \sqrt{\left(\frac{2\pi\nu_0 n}{c_0}\right)^2 - \left(\frac{\pi}{h}\right)^2}$, $\gamma = \sqrt{\left(\frac{\pi}{h}\right)^2 - \left(\frac{2\pi\nu_0}{c_0}\right)^2}$, n the index of the dielectric material, and c_0 the speed of light in vacuum. B_0, B_0' and α are constants, where α is determined by the continuity equation at the surface of the resonator. B_0 and B_0' are related by the normalization of Ψ_0.

In the experiment though we actually have an air-gap between the resonators and the top-plate. We cannot place the top-plate directly onto the resonators, since the resonance frequencies have shown to be very sensitive to the contact condition between the metallic plates and the resonators [45]. Those conditions would vary too much from one resonator to another due to the slightly uneven top-plate and fabrication imperfections within the resonator heights. Leaving an air gap also enables us to scan above the resonators with the loop antenna. Since the air-gap actually breaks the symmetry in the z-direction, we can't separate the variables and solve the Helmholtz equation in the way we did. We assume that the symmetry is still sufficiently maintained, so that we can modify (2) by introducing an effective z-dependency $f(z)$ that respects the boundary conditions $f(0) = f(h) = 0$ and an effective $k_\perp'$ that is defined using the function f [28]. Since the z-dependence inside the resonator is not a perfect sinus anymore, we can expect to couple to the first few radially evanescent modes in z-direction outside the resonator. We get

$$B_z(r,z) \approx B_0'\Psi_0(r,z) = B_0\cdot\begin{cases} f(z)\cdot J_0(k_\perp' r)\cdot\vec{e}_z & \text{for } r<D \\ \sum_m a_m \sin\frac{m\pi z}{h}\cdot K_0(\gamma_m r)\cdot\vec{e}_z & \text{for } r>D \end{cases}, \tag{3}$$

with $\gamma_m = \sqrt{\left(\frac{m\pi}{h}\right)^2 - \left(\frac{2\pi\nu_0}{c}\right)}$ and a_m are constants defined by the continuity equation at the surface of the resonator. Since the loop antenna is sitting at a fixed height z_0 above the resonator, we include the z-dependence and the normalization in new defined coefficients $\alpha_m = a_m \sin(\frac{m\pi}{h}z_0)/f(z_0)$ resulting in [28]

$$\Psi_0(r,z_0) \equiv \Psi_0(r) \propto \begin{cases} J_0(k_\perp' r) & \text{for } r<D \\ \sum_m \alpha_m\cdot K_0(\gamma_m r) & \text{for } r>D \end{cases}. \tag{4}$$

$|\Psi_0(\vec{r}_1)|$ is related to the reflection signal $S_{11}(\nu)$ ($\vec{r}_1$ denoting the position of the antenna) through a Breit-Wigner function, at the vicinity of the resonance ν_0, as follows [28]:

$$S_{11}(\nu) = 1 - i\sigma\frac{|\Psi(\vec{r}_1)|^2}{\nu - \nu_0 + i\Gamma} \tag{5}$$

where σ is a coupling term slowly varying with the frequency that is depending on the used antenna. For the frequency range we are working in, we suppose it to be constant [46]. Γ corresponds to the spectral width of the resonance essentially due to Ohmic losses ($\sigma << \Gamma$). Fitting the complex reflection S_{11} at the resonance with a complex Lorentzian including a complex linear background to incorporate base line effects, one can extract the complex residua from which the wavefunction $|\Psi(\vec{r}_1)|$ can be extracted up to factor $\sqrt{\sigma}$. To retrieve the sign of the wave

Optical Materials EXPRESS

function a second antenna needs to be added and the transmission measurements evaluated (see Section 6 and Eq. (12)). As this invokes an additional perturbation of the system by the second antenna this will be only added if necessary.

For Sections 3 and 4 we use resonators with a diameter $D = 6\,\text{mm}$, but the obtained results can be transferred directly to the other resonator series. Figure 2 shows the spectrum and wavefunction $\Psi_0(r)$ of a single resonator, that was extracted from reflection measurements, where the loop-antenna was moved by 0.1 mm-step above a straight line passing through the center of the resonator. One can note that $\Psi_0(r)$ is changing its sign outside of the resonator. Since a reflection measurement cannot give us access to the sign of the wavefunction, we compared the wavefunction $|\Psi_0(r)|$ extracted form the reflection experiment with the loop antenna to the wavefunction extracted from a transmission experiment using a second antenna, where we actually can access the phase of the wavefunction and thus directly see the change of sign (see Section 6 for more details on transmission-measurements). Since each antenna is a perturbation to the system, we decide to use $|\Psi_0(r)|$ extracted from the reflection measurement and manually change its sign at exactly the positions where the resonances are vanishing. We fit the extracted single disk wavefunction $\Psi_0(r)$ using (4) up to the order $m = 4$. Including higher orders does not improve the fit anymore. The fit parameters are indicated in the figure caption. Since the loop antenna is not a point-like antenna, it is integrating over a small surface therefore leading to effective parameters.

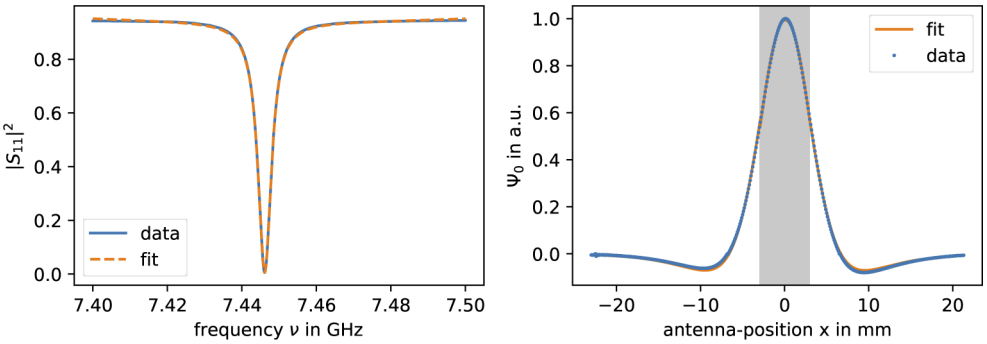

Fig. 2. (left) Reflection spectrum of single resonator, measured with the loop antenna over the center of the resonators. We fit it with a Lorentz line to find its resonance frequency $\nu_0 = 6.446\,\text{GHz}$ and width $\gamma = 2.2\,\text{MHz}$. (right) Extracted single resonator wavefunction Ψ_0 measured on a line going through the center of the resonator. Inside the resonator, corresponding to the gray zone, we fit it with $f(x) = A \cdot J_0(\gamma' x)$ and outside of the resonator with $f(x) = \sum_{i=1}^{4} a_i \cdot K_0(\gamma_i x)$, where $\gamma_i = \sqrt{\left(\frac{i\pi}{h}\right)^2 - \left(\frac{2\pi\nu_0}{c}\right)}$ is defined using the measured resonance frequency ν_0. The obtained fit parameters are $A = 0.994$, $\gamma' = 0.481\,\text{mm}^{-1}$, $a_1 = -1.47$, $a_2 = 22.3$, $a_3 = -58.2$, $a_4 = 46.9$ and $h = 11.6\,\text{mm}$.

We find a good agreement between the measured resonance and the Lorentz line fit, as well as between the fit-function (4) and the extracted wavefunction. The resonance is well isolated and has a quality factor $Q = \nu_0/\gamma \approx 3000$, which makes it suitable for tight-binding experiments. This quality factor includes losses stemming mainly from Ohmic losses of the induced currents in the top and bottom plates, but as well material losses inside the resonator, and the coupling to the non-resonant TM_0 mode, which can freely propagate between the plates and radiates at the border of the open system. The fitted free parameter $h = 11.6\,\text{mm}$ corresponds reasonably well to the directly measured height of $h_{\text{meas}} \approx 12\,\text{mm}$. The bottom and top plates are not perfectly parallel, leading to an incertitude of a few tenths of a millimeter when measuring directly their distance. One can see that the energy is well localized inside the resonator while outside the

Optical Materials EXPRESS

fields are decreasing fast with increasing distance from the center. This is an important property in order to be able to describe the system with a tight-binding model.

4. Multiple coupled resonators–beyond tight-binding description

Apart from the energy well localized inside the resonators, another important step towards a tight-binding description is the coupling between resonators. Bringing two resonators closer than a few diameters leads to a coupling that is depending on the separation d of the resonators, due to the evanescent nature of the excited mode outside the dielectric medium, as can be seen in Fig. 3. According to the tight-binding approach the frequency split $\Delta\nu$ equals two times the coupling strength $|t|$ and can be calculated evaluating the overlap integral of the evanescent fields

$$t = \int \Psi^*(\vec{r}) H \Psi(\vec{r} + \vec{d}) \mathrm{d}\vec{r} \tag{6}$$

where $H = -\vec{\nabla}^2/n^2(\vec{r})$ is the 'Hamiltonian' of a scalar wave equation, and $\Psi(\vec{r})$ is the 3D wavefunction of the system [43]. However our setup only allows us to measure 2D scalar wavefunctions $\Psi(x, y, z_0)$, making it impossible to evaluate (6) exactly. Note here that in order to perform tight-binding experiments with our platform, we don't actually need an explicit function $|t(d)|$ since $|t|$ can be easily measured for any distance d and even a simple exponential fit works well to extract intermediate values [44,45]. We nevertheless fit the coupling $|t|$ as a function of the separation d with a strongly simplified approximation of (6), taking into account only the first order evanescent mode outside, and replace the integration by a point-like evaluation in the exact center between the resonators:

$$t \simeq -\Psi\left(r = -\tfrac{d}{2}, z = z_0\right) \frac{\mathrm{d}^2\Psi\left(r = \frac{d}{2}, z = z_0\right)}{\mathrm{d}r^2} \approx K_0\left(\gamma_1 \tfrac{d}{2}\right) \cdot \left[K_2\left(\gamma_1 \tfrac{d}{2}\right) + K_0\left(\gamma_1 \tfrac{d}{2}\right)\right], \tag{7}$$

where K_0, K_2 are Bessel functions. Since the two resonators have slightly different eigenfrequencies due to the fabrication process, we compensate for this by adding a constant frequency shift $\Delta\nu_0$ to the fit function $|t(d)| = A \cdot \{K_0(\gamma_1 d/2) \cdot [K_2(\gamma_1 d/2) + K_0(\gamma_1 d/2)]\} + \Delta\nu_0$. We only fit the two parameters A and $\Delta\nu_0$. We especially re-use the decay constant γ_1 obtained by fitting the outside part of a single resonator, in order to explicitly link the evanescent decay of the single resonator wavefunction to the coupling for increasing distance d. As one can see in Fig. 3 we find a good agreement between the experimental data and the fit-function. Note that the constant frequency shift $\Delta\nu_0 = 1.55\,\mathrm{MHz}$ we found is smaller than the single resonator resonance width $\gamma = 2.2\,\mathrm{MHz}$, meaning that the two used resonators have close enough resonance frequencies.

Another important requirement in order to describe our system with a tight-binding formalism, is that the wavefunctions of the system should be well approximated by superpositions of the single resonators wavefunctions. Still working with the two-resonator system, writing the tight-binding Hamiltonian under the form of a 2x2 matrix (for real only coupling)

$$H = \begin{pmatrix} \nu_0 & -t \\ -t & \nu_0 \end{pmatrix} \tag{8}$$

we find the two eigenvectors $(1, 1)/\sqrt{2}$ and $(1, -1)/\sqrt{2}$ corresponding to the eigenvalues $\nu_0 - t$ and $\nu_0 + t$ respectively. We thus expect a symmetric wavefunction $\Psi_{sym}(r) \propto \Psi_0(r) + \Psi_0(r - d)$ and an anti-symmetric wavefunction $\Psi_{antisym}(r) \propto \Psi_0(r) - \Psi_0(r - d)$.

Similar to the wavefunction scan of a single resonator we perform a series of reflection measurements along an axis going through the center of both resonators. For each antenna-position we then fit the spectra with the superposition of two Lorentz lines in order to extract

Optical Materials EXPRESS

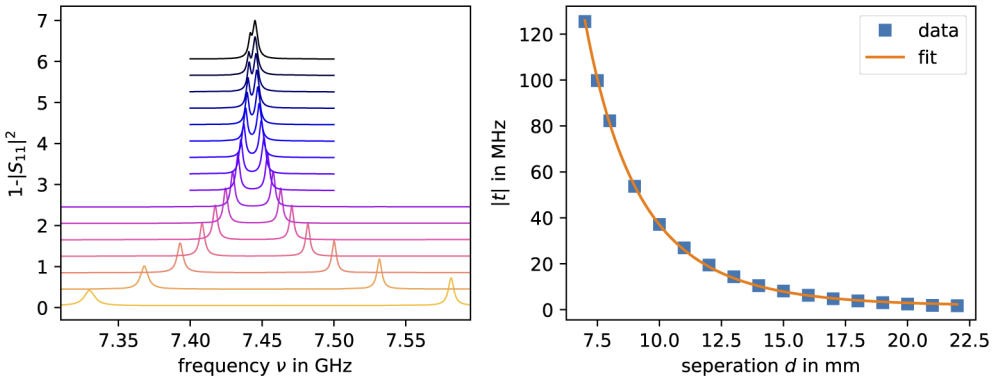

Fig. 3. (left) Reflection spectra of two coupled resonators for different separations d, ranging from 7 mm to 22 mm, with a step-size of 1 mm, that are up-shifted for increasing distance between the resonators. The spectra are measured via the loop antenna over the center of the first resonator. (right) Measured coupling strength $|t|$ as a function of the separation d. We extract $|t| = \Delta\nu/2$ by fitting each spectrum with the superposition of two Lorentz lines in order to find the frequency-split $\Delta\nu$. We then fit $|t|$ with the function $|t(d)| = A \cdot \{K_0(\gamma_1 d/2) \cdot [K_2(\gamma_1 d/2) + K_0(\gamma_1 d/2)]\} + \Delta\nu_0$. The obtained fit parameters are $\Delta\nu_0 = 1.55$ MHz and $A = 63.2$ MHz.

the two wavefunctions Ψ_{sym} and $\Psi_{antisym}$. In Fig. 4 one can see the measured wavefunction intensities for two resonators that are separated by a distance of $d = 10$ mm. We proceed to fit them with functions $f(x) = |A \cdot \Psi_{0,\mathrm{fit}}(x - x_1) \pm B \cdot \Psi_{0,\mathrm{fit}}(x - x_2)|^2$, where $\Psi_{0,\mathrm{fit}}(x)$ is the fit function obatined by fitting the wavefunction of a single resonator (see Fig. 2). Since our two resonators are not identical, we allow $A \neq B$ to compensate for that. We find a good agreement with the measurements, especially since the difference in fitted positions x_1, x_2 equals 10.0 mm, the exact spacing between the resonators. One may note that the antisymmetric state is occurring at the lower frequency and the symmetric state at the higher frequency, indicating that in our system the coupling-strength t is actually negative.

Finding a good agreement in describing a simple two-resonator system by a tight-binding formalism in the frequency-domain, as well as in describing its wavefunctions as symmetric and antisymmetric superpositions, we proceed now to investigate the next more complex system: a linear chain of equally spaced resonators.

We chose to investigate two chains in detail, one with $N = 8$ and one with $N = 7$ resonators. The resonators are separated by a distance of $d = 9$ mm. As in the previous measurements, we measure the reflection along an axis passing through the centers of the resonators, in order to extract the spatially resolved wavefunctions of the N states of the system. In Fig. 5(a-d) we present two reflection spectra for each chain. For the chain with $N = 8$ ($N = 7$) resonators, we present the reflection measured exactly above the first (first) and third (forth) resonator. In the spectra measured above the first resonator, we can identify N distinct and well isolated resonances for both chains. In the spectra above the third (forth) resonator one can see that several resonances are vanishing, since the associated wavefunctions have nodes at that resonator. We compare the spectra with the eigenvalues ν_n of the tight-binding Hamiltonian

$$H_0 = \sum_{i=1}^{N} \nu_0 |i\rangle\langle i| + \sum_{i=1}^{N-1} t|i\rangle\langle i+1| + C.C \tag{9}$$

and find a good agreement. We re-use the single resonator resonance frequency $\nu_0 = 7.446$ GHz (see Fig. 2) and $t = -53.0$ MHz, corresponding to the separation of 9 mm (see Fig. 3).

Optical Materials EXPRESS

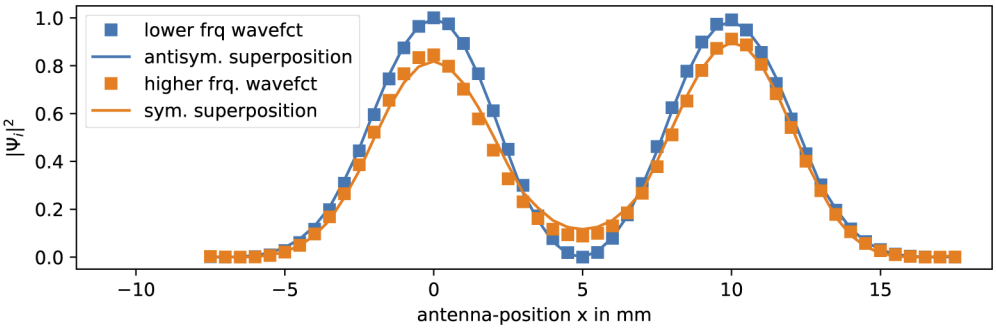

Fig. 4. Extracted wavefunctions of two coupled resonators with a separation of $d = 10\,\text{mm}$ between them (blue/orange squares). The blue squares correspond to the state that is occurring at the lower frequency. The orange squares correspond to the state that is occurring at the higher frequency. We identify the lower frequency state (blue) as the antisymmetric state, since its wavefunction is vanishing at the middle distance between the two resonators. It follows that the higher frequency state is the symmetric state. We then proceed to fit both wavefunction with symmetric and antisymmetric superpositions of the single resonator wavefunction $f(x) = |A \cdot \Psi_{0,\text{fit}}(x - x_1) \pm B \cdot \Psi_{0,\text{fit}}(x - x_2)|^2$ (solid blue/orange lines). The found fit-parameters for the antisymmetric, symmetric superposition are $A = 0.69$, $B = 0.68$, $x_1 = 0.0\,\text{mm}$, $x_2 = 10.0\,\text{mm}$ and $A = 0.71$, $B = 0.75$, $x_1 = 0.0\,\text{mm}$, $x_2 = 10.0\,\text{mm}$.

We then extract the wavefunctions for each state again by fitting each resonance individually with a Lorentz line and present them by pairs of symmetric and antisymmetric states [see Fig. 5(e-l)]. We further search to link the measured amplitude over a resonator to the tight-binding coefficient of that site. One problem that we encounter is the slight overlap of adjacent single resonator wavefunctions, meaning that the measured amplitude $\Psi(r_0)$ over the center of a resonator at position r_0 is not only proportional to a_0, the tight-binding coefficient of that site, but is actually proportional to $\Psi(r_0) = a_0\Psi_0(0) + \sum_i a_i\Psi_0(r_0 - r_i)$, where $\sum_i$ is the sum over the other resonators of the system and a_i and r_i their tight-binding coefficients and positions. This effect changes for each system and especially for each wavefunction individually. In order to illustrate and estimate the deviation we add the eigenstates $|v_n\rangle$ of the tight-binding Hamiltonian (9) as black circles to Fig. 5(e-l). In general, the biggest difference can be observed when comparing the complete symmetric with the complete antisymmetric wavefunctions of a system [see Fig. 5(e-f)], where the deviation is of the order of 10 %.

We still find a very good overall agreement of the general structure of the different wavefunctions, but nevertheless we go one step further and compare our measurement with effective Hamiltonian simulations, that can account for the overlapping single resonator wavefunctions. The effective Hamiltonian theory has been introduced to describe open quantum system and suits perfectly to model our open tight-binding system (an overview is given in Ref. [47]). For a system, where the openness is modeled via only one channel, the effective Hamiltonian takes the form [46,48]

$$H_{\text{eff}} = H_0 - \frac{\mathrm{i}\sigma}{2} WW^T\,, \tag{10}$$

where W is a normalized vector of size N, containing the information on the exact nature of the coupling. σ is the overall coupling strength of the channel and H_0 is a $N \times N$ matrix representing the Hamiltonian of the corresponding closed (tight-binding) system (in our case N corresponds to the number of resonators). Modeling an excitation over the i-th resonator, not taking the overlap of the wavefunctions into consideration, only the i-th element of W is non zero and equals one. In our case the antenna is not only exciting the resonator at site i but also the neighboring sites, since their single resonator wavefunctions have not yet vanished completely at that distance. In

Optical Materials EXPRESS

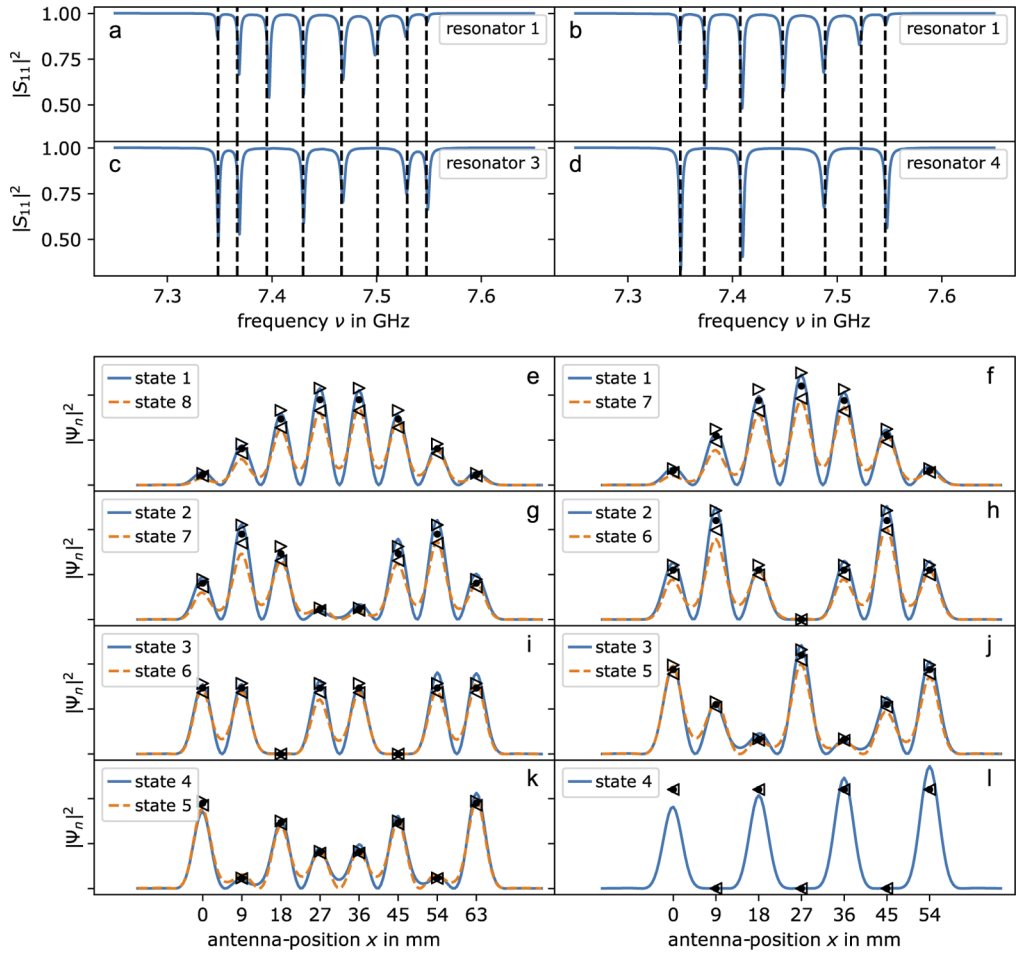

Fig. 5. The figures on the left (right) are corresponding to a chain with $N = 8$ ($N = 7$) resonators.(a),(b) are reflection spectra measured over the first resonator of the chains. (c) and (d) are reflection spectra measured over the third and forth resonator respectively. The dashed lines in (a) -(d) are presenting the eigenvalues ν_n of H_0. (e) to (l) are showing the extracted wavefunctions of the systems as a function of the antenna-position (blue and orange solid lines), as well as effective Hamiltonian simulations as left (higher frequency states) and right (lower frequency states) pointing triangles. The states are numbered increasingly according to their resonance-frequency. If existing, each time the antisymmetric and symmetric state are presented in the same graph. We add the projection $|\langle i|\nu_n\rangle|^2$ of the eigenstates $|\nu_n\rangle$ of H_0 onto the i-th site as black circles at the i-th resonator position (the x-axis ticks correspond to the resonator positions). The measured wavefunctions and effective Hamiltonian simulations share the same y-axis, while the projection of the eigenstates of H_0 were adjusted by a global factor, to match the effective Hamiltonian simulations in (l), since for that state, the effective Hamiltonian simulation should be proportional to the eigenstate of H_0 since there is no contribution from directly neighboring sites, since every other resonator has zero amplitude.

Optical Materials EXPRESS

order to model such an excitation we add a small term ϵ ($\epsilon \ll 1$) on the neighboring sites of the i-th element in W: $W = (\cdots, 0, 0, 1, 0, 0, \ldots) \rightarrow W = (\cdots, 0, \epsilon, 1, \epsilon, 0, \ldots)/\sqrt{1+2\epsilon^2}$. We further neglect next-nearest-neighbor contributions. We set $\epsilon \approx \Psi_0(0)/\Psi_0(d)$, where d is the distance between the resonators, which in our case turns out to be negative, since the measured single resonator wavefunction is negative at a distance of $d = 9$ mm from the center.

The resulting reflection spectrum S_{11} as a function of the frequency ν is then given by [46,48,49]

$$S_{11}(\nu) = 1 - \mathrm{i}\sigma \left(W^T \frac{1}{\nu - H_{eff}} W \right) \tag{11}$$

We simulate the spectra over each resonator and extract the wavefunction the same way as for the measured spectra. The results are presented as triangles in Fig. 5. In order to match the measurements we are using $\sigma = 2.2$ MHz and $\epsilon = -0.035$. ϵ does not correspond exactly to $\Psi_0(0)/\Psi_0(d) = -0.066$, but is the same order of magnitude. The difference can probably be explained by the fact that the antenna is not point-like, thus inducing a convolution operation, that is not commuting with the square-operation (in reflection measurement we only have direct access to $|\Psi|^2$). Apart from local fluctuations (due to small differences of the used resonators), we find a good agreement between the measured wavefunctions and the ones simulated using the effective Hamiltonian. The wavefunction of state 4 for the chain with $N = 7$ resonators [see Fig. 5(l)] actually shows a tendency of growing peak height for an increasing antenna position. This is probably due to not perfectly parallel bottom and top plates, leading to different heights for different areas of the chain changing slightly the resonance-frequencies and couplings between the resonators. Since state 4 is occurring at the single resonator resonance frequency, we expect it to be the most sensitive one to those local fluctuations.

5. Anisotropic coupling

Since the fundamental TE_1 s-mode is the most robust and well isolated mode, up to now we were working only with it. The resonators though are showing more TE-modes within the cut-off frequency range of the cavity [44]. We proceed to investigate the p-mode since its spatial shape provides anisotropic coupling. These high order orbitals have been successfully exploited in topological experiments using polaritons [12,50]. In this paper we chose to only present preliminary measurements in order to demonstrate the possibility of our platform. Depending on their diameter, certain resonator series are better suited than others, since we need a well isolated resonance to work with. We chose to perform these measurements with resonators with $D = 8$ mm. Indeed, with $D = 6$ mm, the TE_2 s-mode with second order z-dependency is too close to the TE_1 p-mode with fundamental z-dependency due to its similar height and diameter.

As one can see in Fig. 6, the spectrum of the p-mode of a single resonator shows a well isolated resonance. Adding a second resonator at a distance of 10 mm splits the one peak into four, indicating that the single resonator level is actually degenerate. Due to fabrication imperfections we don't expect the two orthogonal p-modes to be at exactly the same frequency. Nevertheless the observed resonance in the single resonator spectrum can be well fitted with a single Lorentz line, meaning that the frequency difference is significantly smaller then the resonance width, and the two states are almost perfectly degenerate. The fact that we observe four individual peaks in the two-resonator reflection spectrum confirms the expected anisotropic coupling, that arises from different overlap integrals depending on the alignment of the modes compared to the axis going through the center of both resonators. We proceed to extract the wavefunctions of the four different states by performing a full two dimensional reflection scan with the loop antenna. Instead of fitting each resonance for each position individually to extract its wavefunction (as done in the previous chapters) we use $1 - |S_{11}(\nu)|^2$ as an approximation of the local density of states $\rho(\vec{r}, \nu)$ for each antenna-position $\vec{r}$ [28,44,49]. By integrating along the frequency axis around each peak $\rho(\vec{r}, \nu)$ we find a good approximation of $|\Psi(\vec{r})|^2$). The obtained two dimensional

Optical Materials EXPRESS

wavefunctions are plotted in Fig. 6(a-d). One can clearly identify the two orthogonal p-modes of the single resonators that form either a symmetric or antisymmetric superposition: The one where the nodal lines are parallel to the axis going through the centers of both resonators (b,c), and the one, where the nodal lines are orthogonal to that axis (a,d). One can identify the two higher frequency modes as symmetric and the two lower frequency modes as antisymmetric superpositions. This corresponds to the results observed for the s-mode (see Section 3 and 4). Since the single resonator p-mode wavefunction is extending further outside of the resonator along the axis that is perpendicular to the modal line, we find the two modes that are coupled via their overlap along that dia rection at the extremes of the spectrum, since their overlap and thus the resulting coupling strength is greater. For the two-resonator system the degeneracy was lifted due to the anisotropic coupling along the axis going through the centers of both resonators. In order to perform measurements with more complex structures, that are e.g. symmetric in both the $x-$ and $y-$direction where the degeneracy will persist, one needs precise control exciting the p-modes with the desired polarization. For our platform this can be done via a precise positioning and orientation of a kink antenna, that is coupled only to one of the two modes or placing an elongated metallic object on top of the resonator to force a nodal line and thus orient the p-mode along that direction.

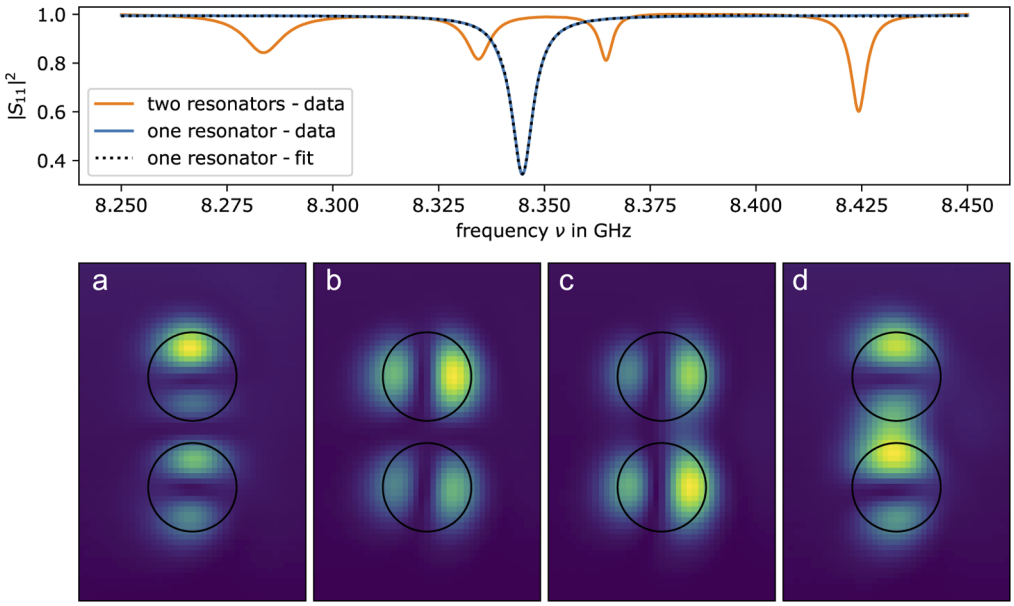

Fig. 6. (top) Reflection measurement for a single resonator (blue) and two coupled resonators (orange) separated by a distance of 10 mm (from center to center) measured at $dx = dy = 3$ mm from the center of the (first) resonator. The single resonator spectrum was fitted with a Lorentz line (black dashed line). (a - d) two dimensional wavefunctions $|\Psi|^2$ of the two resonator system (ordered according to their frequency). The black circles are corresponding to the perimeters of the two resonators.

6. Time domain

Up to know we were only presenting reflection measurements. They only use one antenna, are thus faster to perform and show very good results extracting the (local) density of states and wavefunction intensities. In reflection measurements though one looses the information about the phases of the wavefunctions and there can be systems where one is explicitly interested in

Optical Materials EXPRESS

these quantities. Here transmission measurements come into play. The transmission S_{12} between two weakly coupled point-like antennas at positions $\vec{r}_1$ and $\vec{r}_2$ for a system with N states can be written as [46]

$$S_{12}(\nu;\vec{r}_1,\vec{r}_2) = -\mathrm{i}\sqrt{\sigma_1\sigma_2}\sum_n^N \frac{\Psi_n(\vec{r}_1)\Psi_n^*(\vec{r}_2)}{\nu-\nu_n+\mathrm{i}\Gamma_n}, \tag{12}$$

where $\Psi_n(\vec{r})$, ν_n and Γ_n are the wavefunction, resonance frequency and resonance width of state n. σ_1 (σ_2) is the coupling strength of antenna 1(2), that we suppose to be constant within the frequency range we are working in and the same for all states [46]. Having one fixed antenna at position $\vec{r}_1$ and one moving antenna, one can extract the wavefunctions $\Psi_n(\vec{r}_2)$ up to global factor $\Psi_n^*(\vec{r}_1)\sqrt{\sigma_1\sigma_2}$ for any position $\vec{r}_2$ of the scanning antenna by fitting the complex resonances in S_{12}.

In Fig. 7 one can see the transmission spectra of a benzene ring, measured between a fixed kink antenna and the movable loop-antenna, that was successively placed above the centers of all 6 resonators. Fitting the two outermost resonances one can extract the complex amplitudes of the associated wavefunctions up to a global phase factor. Since for this system we expect real only wavefunctions, we subtract a global phase from the extracted complex amplitudes in order to minimize the overall imaginary part (remaining imaginary part is less then 5 % of the real part for all sites) and then plot its projection onto the real axis [see Fig. 7(a)]. One can clearly distinguish between the complete symmetric (at the highest frequency) and complete antisymmetric state (at the lowest frequency).

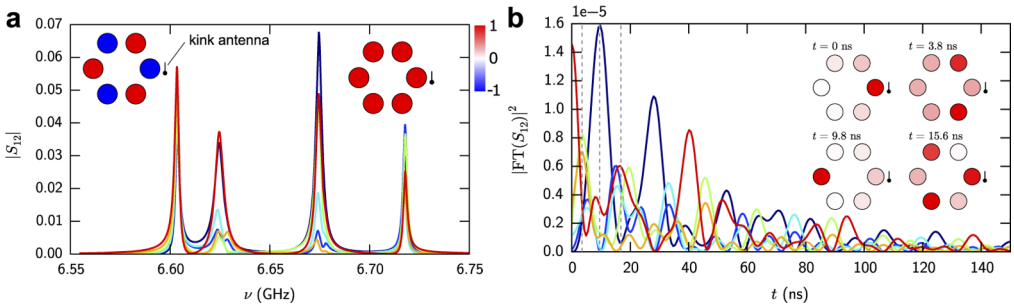

Fig. 7. (a) Transmission spectra measured between a fixed kink antenna and the movable loop-antenna successively placed above each resonator and its Fourier transforms (b). Each color corresponds to a different site/resonator. The insets in (a) show the amplitudes of the wavefunctions for the highest and lowest frequency state. The insets in (b) show snapshots of the temporal intensity evolution at times t = 0 ns, 3.8 ns, 9.8 ns and 15.6 ns. These times are additionally marked as vertical dashed lines in (b). All inset plots were normalized so that the maximum value equals 1 in order to use the same color scale for both set of inset-plots in (a) and (b).

Another equivalent way to exploit the transmission spectra is by calculating its Fourier transform $FT(S_{12})$ and link it to the temporal intensity distribution $I(t,\vec{r}) \propto |FT\left[S_{12}(\nu,\vec{r})\right]|^2$. One is thus able to visualize the dynamics of a pulse spreading from the fixed antenna into the system as shown in Fig. 7(b), and as used in Section 7.1.

7. Investigation of topological systems by coupled microwave resonator lattices

In the realm of topological photonics, our microwave experimental platform has been successfully implemented in various situations: in 1D systems with broken passive $\mathcal{PT}$ symmetry (Subsection 7.1), in 2D systems either with partial chiral symmetry breaking (Subsection 7.3), or with an

Optical Materials EXPRESS

uni-axial deformation of the lattice (Subsection 7.2), or even with non homogeneous deformation (Subsection 7.4). All these systems rely on linear wave propagation, while in the following Section 8 a strategy based on the interplay between topological protection and nonlinearity is illustrated.

7.1. Topological interface state in a non-Hermitian system with broken $\mathcal{PT}$ symmetry

The SSH model (Su, Schrieffer and Heeger [51]) constitutes the minimal one-dimensional model with a topological band structure. This bipartite lattice with staggering hopping amplitudes was originally introduced in an electronic context to describe fractionalized charges in polyacetylene, which appear in the presence of a dimerization defect. In absence of the defect, this dimer model has attracted independent attention because it provides a natural platform for gain-loss distributed systems displaying a so-called parity-time ($\mathcal{PT}$) symmetry [52–56]. As shown in Fig. 8(a), this model can be easily implemented in our experimental platform: alternating couplings are realized by alternating distances, and absorptive patches placed on one of the two sublattices allow to implement a passive variant of non-Hermitian $\mathcal{PT}$ symmetry [35]. By repeating one spacing in the center of the chain, one introduces a defect that breaks the $\mathcal{PT}$ symmetry. Due to this symmetry breaking, as one can see in Fig. 8(d), a mode appears at the center of the spectral gap, that we call "zero-modes" in reference to the "zero-energy" modes in condensed-matter context. As shown in Fig. 8(e), the corresponding wavefunction is spatially localized on the interface created by the defect and contrary to the other "bulk"- modes of the chain confined to a sublattice. Moreover, as the defect imposes a gauge prescription, both parts of the chain acquire a different topological charge, namely the Zak phase [57]. The interface state is thus topologically protected and inherits the properties of robustness against disorder [35].

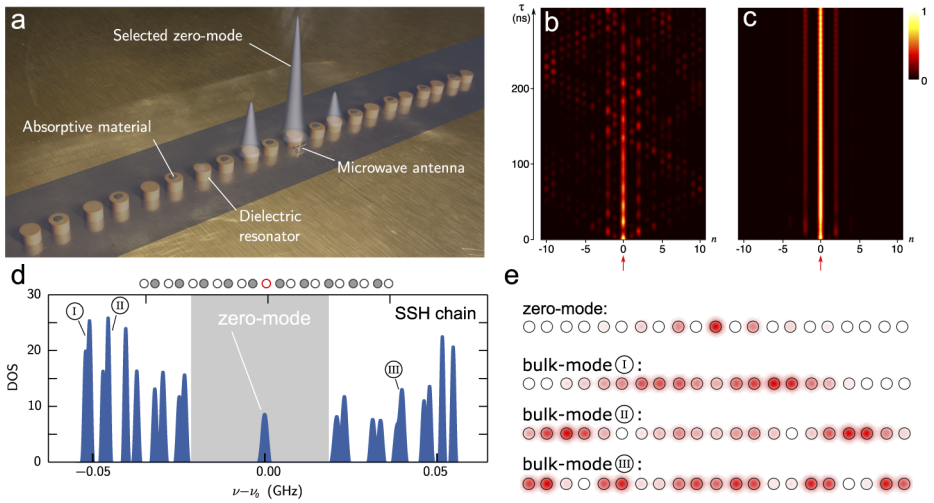

Fig. 8. (a) Microwave realization of a SSH chain with passive non-Hermitian $\mathcal{PT}$ symmetry breaking. Time evolution of a pulse launched on the defect site. (b) Without absorption, diffraction and interference spoil the propagation of the interface state, which cannot be discerned after 250 ns. (c) With staggered losses, the visibility of the interface state is drastically enhanced. (d) Experimentally obtained density of states (DOS) of the chain. One can clearly identify the zero-mode in the center of the band-gap (grey zone). (e) Spatial distribution of the zero-mode and a selection of bulk-states. The associated peaks in the DOS (d) are referenced using encircled roman numbers. Adapted from Ref. [35].

As a consequence of the $\mathcal{PT}$ symmetry breaking, the interface state is not affected by the staggered losses and then become the predominant mode in the spectrum. This feature is

Optical Materials EXPRESS

illustrated in the time evolution of a pulse injected in the defect resonator as shown in Fig. 8 for the two situations: (b) without absorption and (c) with staggered losses. In the first case, the propagation of the interface state is dramatically degraded by diffraction and interference. The 'bulk' states even if not predominantly excited by the initial condition participate to the dynamics. On the contrary, losses induce a selective enhancement of the interface state which now dominates the propagation without any degradation.

7.2. Topological phase transition and edge state engineering in strained honeycomb lattices

For almost two decades the exciting physics of graphene has stimulated intense research activities [58,59]. Graphene has become the paradigm of a larger class of "Dirac materials" whose fundamental interest and promise of applications are attracting a lot of consideration [60,61]. One of the most fascinating aspects for the scientific community is the physics of well-celebrated Dirac points. In their vicinity relativistic physics became accessible on table-top condensed-matter experiments [62]. In addition, while the topology of graphene is trivial, the Dirac points are characterized by opposite topological charges (opposite Berry phases). The richness of the low energy physics close to the Dirac points lies essentially in the honeycomb structure. The latter can be built in various (meta) materials, responding to various types of wave excitations. Thus exploring achievements arising from many experimental realization using artificial graphene based on atoms, molecules and photons [63,64], mechanical systems [65], in acoustic [66–68], and in elastodynamics [69]. Among them, our setup is probably one of the most flexible as we have almost total freedom in the placement of the resonators. It was thus possible to carry out a true engineering of the Dirac points [39].

By exerting an uniaxial strain on a honeycomb lattice, and consequently introducing an anisotropy in the couplings, the Dirac points move along a specific direction in the Brillouin zone. Depending on the direction of the strain axis with respect to the lattice vectors, the Dirac points can move towards each other, merge and finally the two opposite topological charges annihilate: the system experiences a topological phase transition [70,71]. If the anisotropy is increased further, a band gap opens in the dispersion relation. This transition from a gapless (Dirac) phase to a gapped phase corresponds to a Lifshitz phase transition from a semi-metallic to an insulating phase. The left row of Fig. 9 shows a regular honeycomb lattice with an hexagonal shape and only armchair boundaries and two deformed lattices. The strain is applied along the vertical direction, which corresponds to one lattice axis. Thus the strain changes one of the three nearest-neighbor couplings only (in this study the role of the highest-order nearest-neighbor couplings are qualitatively inessential). The modified coupling is denoted by t' and the anisotropy parameter by $\beta = t'/t$. In the experiments, β is gradually increased from 1, corresponding to the isotropic case, to 3.5, where the system is supposed to be far in the gapped phase. On the top-right of Fig. 9, we plot the measured density of states (DOS) obtained for six different values of β using a white-blue colorscale. The linear opening of the gap with β above a critical value is emphasized by the gray zone. The topological transition between a gapless phase and a gapped phase is unambiguously observed. These experimental results are successfully compared with the DOS calculated for the corresponding infinite systems with tight-binding parameters extracted from the experiments [39].

In Fig. 9, the DOS was obtained by averaging the reflection measurements over the bulk resonators only (the darkest sites on the left panel), thus avoiding the edges of the deformed hexagons. Without this precaution, additional states would have appeared around the Dirac frequency, at the center of the gap, characterizing the topological transition. These edge states have been first predicted in graphene ribbons [72–74] and later observed along "zigzag" edges [75,76]. Although not strictly speaking topologically protected, edge states in graphene possess

Optical Materials EXPRESS

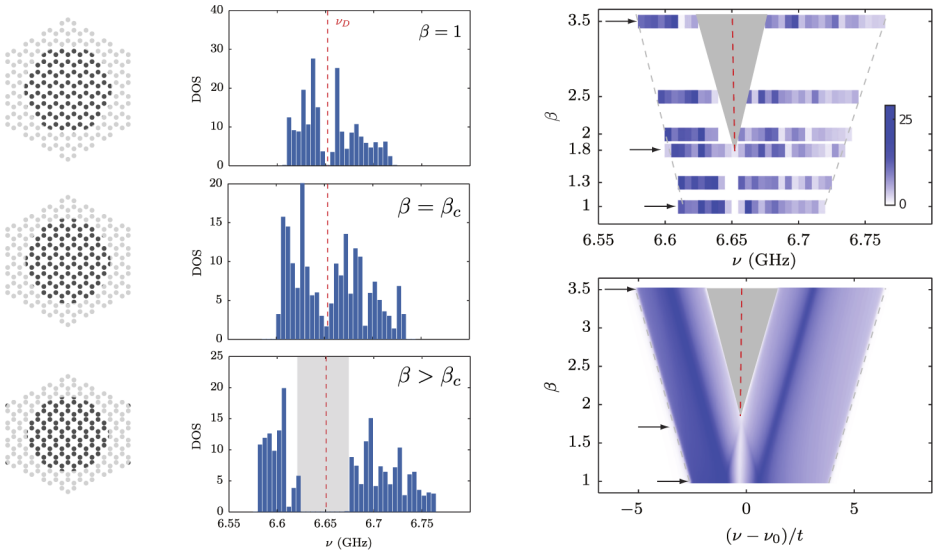

Fig. 9. (left row) 3 deformations of the microwave honeycomb lattice (the strain is applied along the vertical axis): (top) isotropic case, (middle) critical anisotropy corresponding to the topological transition, (bottom) larger strain. In dark the sites over which the local densities of states are averaging to obtain the density of states. (middle row) The corresponding density of states. (right row) (top) The experimentally measured density of states in color plot for different values of the anisotropy parameter β (the arrows indicated the situations depicted in the middle), (bottom) tight-binding calculation of the DOS for an infinite systems with the values of the couplings taken from the experiments. Adapted from Ref. [39].

a topological origin coined by the Zak phase and remain robust against weak chiral symmetry perturbations [77,78].

In Ref. [40], we proposed an experimental manipulation of edge state properties by applying uniaxial strains on an artificial graphene ribbon exhibiting the three usual types of edges, namely zigzag, bearded and armchair. The lattice is presented at the top of Fig. 10. The strain is applied along a direction parallel to the armchair edges, which corresponds to one lattice axis. Thus the strain changes one of the three nearest-neighbor couplings only, denoted by t'. Note, that in this study higher-order nearest-neighbor couplings are qualitatively inessential. Whatever the anisotropy $\beta = t'/t$ is, the two armchair edges along the strain axis do not support any edge state [78].

For different values of the anisotropy parameter β, Fig. 10(a-d) show the spatial intensities distribution associated to modes at the Dirac frequency – close to the bare frequency of each isolated resonator [28] – that we call "zero-modes" in reference to the "zero-energy" modes in condensed-matter context. Both zigzag and bearded edges are populated in the unstrained case $\beta = 1$ [Fig. 10(b)]. When a strain is applied ($\beta \neq 1$), the relative strength of the two types of zero-modes is controlled by the value of β. For $\beta = 0.4$ [Fig. 10(a)], bearded edges are dominant whereas they are totally absent for $\beta = 2.5$ where only the zigzag edge is found [Fig. 10(d)]. For intermediate anisotropy [$\beta = 1.5$, Fig. 10(c)], both edge types are seen, with an opposite relative strength compared to the $\beta = 1$ case. Note that the topological phase transition described above occurs at $\beta_c = 1.8$. The existence of edge states is thus not determined by the topological transition observed in [39] but more subtly to the motion of the Dirac points in the Brillouin zone when the lattice is deformed according to β [70,71]. Indeed, their relative weight and their extension into the bulk is completely controlled by the anisotropy parameter [40]. As also pointed

Optical Materials EXPRESS

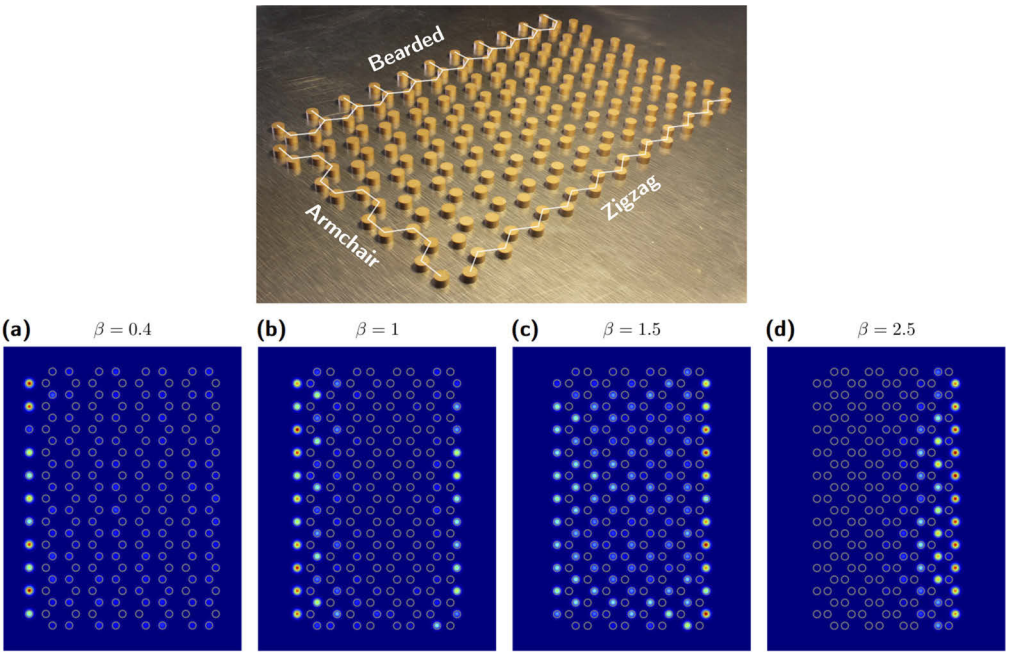

Fig. 10. (top) Picture of an unstrained artificial graphene ribbon with zigzag, bearded and armchair edges. Experimental zero-mode intensities for different anisotropy parameters (a) $\beta = 0.4$, (b) $\beta = 1$ (unstrained honeycomb lattice), (c) $\beta = 1.5$ and (d) $\beta = 2.5$, the anisotropy axis being along the parallel armchair edges, the zigzag edge is on the right, and the bearded on the left. Adapted from Ref. [40].

out in [79], their existence is a manifestation of the non zero value of the Zak phase. This 1D winding number has been directly measured in cold atom experiments [80].

7.3. Partial chiral symmetry breaking

In the previous studies based on deformed honeycomb lattices, the role of high-order nearest-neighbor couplings, always present in our experiments, are not qualitatively important. Their influence is simply expressed by a renormalization of some pertinent parameters. For example, in the topological phase transition in strained graphene, the critical anisotropy, expected at $\beta_c = 2$ for tight-binding with nearest-neighbors couplings, is lowered to $\beta_c = 1.8$ because of the third order nearest-neighbor couplings. In [81] we exploited this long range couplings to induce a partial breaking of chiral symmetry in a two-dimensional bipartite system possessing flat band and to stabilize and isolate point-defect zero-modes.

One of the main goals of present research in electronic and photonic systems is the realisation of topologically protected states [4,11,82]. The existence of such states relies on symmetries, with the present focus set on the roles of time-reversal symmetry, chiral symmetry and charge-conjugation symmetry. In combination with considerations of dimensionality, a classification of robust protected states can then be achieved, which guides the design of theoretical models and experimental realizations [83]. In the photonic setting, the most interesting symmetry classes are difficult to realize - e.g., magneto-optical effects to break time-reversal and induce quantum-hall like phases are typically too weak. The chiral symmetry is most easily realized. Indeed, chiral symmetries emerge naturally in bipartite lattices [84,85] with the consequence that they can support robust zero-modes localized at point defects [86], which exhibit sublattice polarization [84,85], while all finite-energy states have an equal weight on both sublattices. As an intriguing

Optical Materials EXPRESS

consequence, many bipartite lattices of interest, such as the Lieb lattice – a face-centered depleted square lattice – exhibit flat bands of zero-modes supported by one of the two sublattices (the majority sublattice, which contains more sites per unit cell than the complementary minority sublattice). Various photonic realizations of regular Lieb lattices tried to exploit the properties of these compacton-like states [87–90].

In Fig. 11(a) the Lieb lattices with its coupling constants is presented. All sites have the same eigenenergies/frequencies and the dimerization is implemented by different nearest-neighbor couplings u, v, u', and u''. Figure 11(b-d) shows the evolution of the band structure of a Lieb lattice with the couplings. Figure 11(b) corresponds to the situation of a regular Lieb lattice with uniform couplings along vertical and horizontal axes only. The band structure consists of a flat band supported by the majority sublattice and two dispersive bands of extended states touching at a Dirac point. When the lattice is dimerized [Fig. 11(c)], the dispersive bands are separated by a gap, while the flat band and the point-defect state remain fixed at zero energy. Figure 11(d) shows the evolution when next-nearest-neighbor couplings (along diagonals w, w', w'', and w''') are introduced: the flat band becomes dispersive and moves to finite energies, the symmetry of the dispersive bands is broken, only the defect state remains unaltered. One can prove that the detuning of the compacton-like states is due to their finite sublattice polarization [81]. The next-nearest-neighbor couplings breaks the chiral symmetry on the majority sublattice, which moves the flat band away from the chiral symmetry point in the spectrum. This leaves behind a spatially localized zero-mode supported by the minority sublattice, on which the chiral symmetry remains operational.

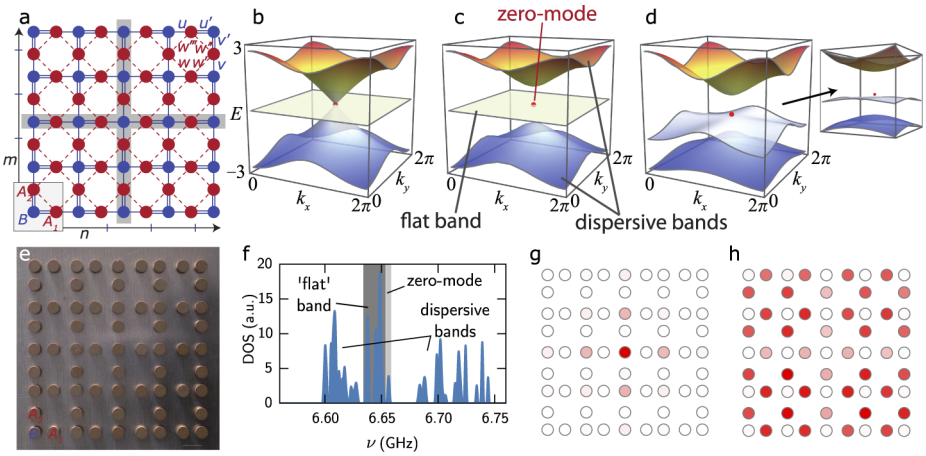

Fig. 11. (top) Theoretical description of the Lieb Lattice. (a) Lieb lattice with nearest-neighbor couplings u, v, u', v', and next-nearest-neighbor couplings w, w', w'', w''' that reduce the chiral symmetry. This lattice realizes a centered dimerization defect (gray zones). (b)–(d) Dispersion relation of the infinite system. The localized zero-mode becomes spectrally isolated as one passes from (b) uniform couplings ($u = v = u' = v'$) over (c) dimerized couplings $u = v = 4/3, u' = v' = 2/3$), gapping out the extended states, to (d) additional next-nearest-neighbor couplings ($w = 0.4, w' = w''' = 0.2, w'' = 0.1$), gapping out the flat band. The inset in (d) details the spectral separation of the zero-mode and the flat band. (bottom) Microwave realization and experimental results. (e) Picture of the experimental microwave realization of the dimerized Lieb lattice. The white bar corresponds to 12 mm. (f) Density of states, with the point-defect zero-mode shaded in light gray and the flat band shaded in dark grey. (g) Spatial distribution of the zero-mode. (h) Spatial distribution of the 'flat' band. Adapted from Ref. [81].

Optical Materials EXPRESS

Figure 11(e-g) shows the experimental results for configurations where the point defect sits at the center of the lattice, and in a situation with semi-chiral symmetry due the next-nearest-neighbor couplings between microwave resonators. The density of states exhibits the expected behavior [see Fig. 11(e)]: The extended bands are not symmetric, the "flat band" acquires a finite width (dark gray zone) and is shifted from the zero energy thus isolating the zero-mode (light gray zone). Note that thus the flat band is not flat anymore and is a standard band with a small dispersion but still the wavefunctions remain confined to the majority sublattice [Fig. 11(f)] but cover the whole lattice. The state associated with the spectrally isolated peak displays a spatially localized profile with intensity confined to the minority sublattice [Fig. 11(g)]. By using the same strategy as the one deployed in Section 7.1, the defect state can be further promoted via judiciously introduced local losses [81]. Our findings introduce a whole new element into considerations of topology and symmetry, which is both of fundamental importance as well as of practical value.

7.4. Giant pseudo-magnetic field

In the celebrated quantum Hall effect, quantum-mechanical effects force electrons exposed to a magnetic field to travel though a conductor in precisely determined numbers [91]. This results in devices with a resistance that does not depend on details, to the extent that it does not matter if the material is perfectly clean – the hallmark of a topological effect [92]. The backbone of this behavior are Landau levels, quantum states where many electrons share the same, well-defined energy, which can be imaged by spectroscopic experiments. Unfortunately, magnetic fields cannot be used to achieve the same effect for light, as this is described quantum mechanically by photons, electrically neutral particles that are insensitive to magnetic fields (albeit magneto-transverse diffusion of light has been observed [93], but the physical mechanism is very different). Consequently, any attempts to observe Landau levels and their peculiar topological properties in photonic systems appear to be in vain. Fortunately, in the wake of the extraordinary research activities triggered by the experimental realization of graphene, it has been recognized that magnetic fields can be mimicked by means of inhomogeneous mechanical strain [94,95]. The effect is then captured by the concept of a pseudo-magnetic field: An artificial gauge field that modifies the low-energy spectrum of graphene near the famous Dirac points, where electrons behave like relativistic particles. This results in the formation of pseudo-Landau levels with the same energies as conventional Landau levels, but subtly different quantum-mechanical wave intensity patterns. This concept has been implemented in a variety of artificial graphene systems, ranging from acoustics [96,97] to photonic devices [9] and exciton, polariton excitations [98]. However, previous works failed to observe the hallmarks of topological protection of the pseudo-Landau levels, partially because the subtly different nature of their topology was not completely understood.

In a recently published paper [41], we overcame these obstacles by combining new theoretical insights into these topological features with direct experimental observations in our microwave platform. The unstrained system forms a honeycomb lattice with nearest-neighbor spacing $a_0 = 13.9\,\mathrm{mm}$, combining two triangular A and B sublattices and forming a triangle with zig-zag edges. The bare resonance frequency of each resonator is $\omega_0 = 6.653\,\mathrm{GHz}$, and the coupling strength between nearest-neighbor sites is $t_0 = 21.5\,\mathrm{MHz}$. To create a pseudo-magnetic field corresponding to that in strained graphene, a triaxial spatial coupling profile is implemented through the following non uniform couplings law:

$$t_l = t_0[1 - (\eta/2a_0^2)\boldsymbol{\rho}_l \cdot \mathbf{r}], \tag{13}$$

where $\mathbf{r}$ refers to the positions of the links between the coupled resonators in the unstrained system and $\boldsymbol{\rho}_l$ are pointing along these coupling directions. Note, that in contrast to the uniaxial strain applied in Section 7.2 this strain breaks the translational lattice symmetry. The topology of the two deformed lattices are thus not equivalent. This coupling profile ensures a constant

Optical Materials EXPRESS

pseudo-magnetic field of strength η throughout the whole system. As illustrated by the blue arrows in Fig. 12, this deformation stretches the system along three directions, corresponding to triaxial strain. Translating the experimental conditions to genuine graphene, we managed to achieve field strengths up to 42000 T, which are unattainable in the original setting. As the strength of this field increased from zero to its maximal value, a radical change of the resonance frequencies and intensity patterns is observed. Sharp peaks appeared in the frequency spectrum, corresponding to well-defined pseudo-Landau levels (Fig. 12).

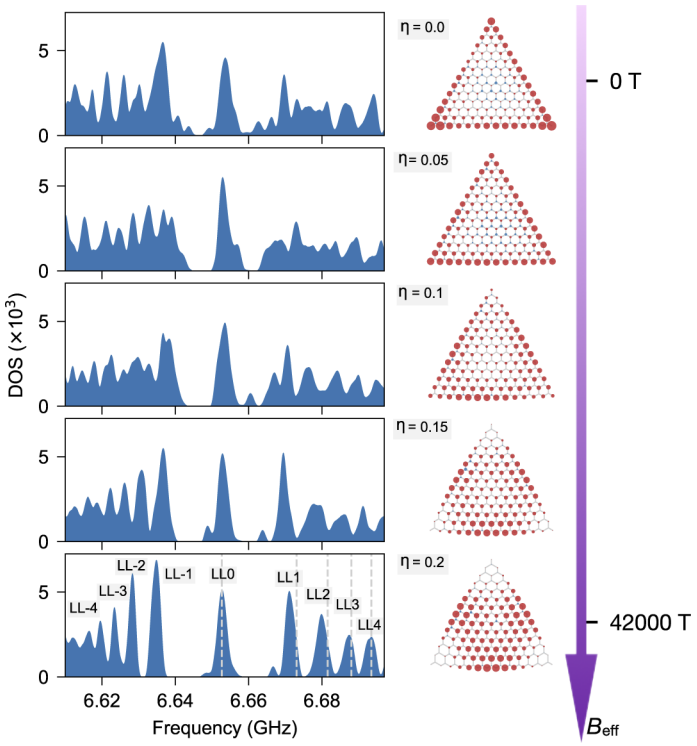

Fig. 12. Experimental density of states (left panels) and microwave intensity distributions of the 0-th order pseudo-Landau level (right panels). The grey dashed lines in the total density of states for $\eta = 0.2$ depict the expected pseudo-Landau level frequencies from coupled-mode theory. The size of the circles corresponds to the intensity on the A sites (red) and B sites (blue). From top to bottom, the pseudo-magnetic field strength η varies from 0 to 0.2, with the maximal value corresponding to 42000T in graphene. In this process, zigzag edge states present in the regular system (top) continuously transform to bulk states (bottom), while remaining confined to one sublattice. Adapted from Ref. [41].

We demonstrated two powerful signatures of topology, relating to two types of pseudo-Landau levels found at different frequencies. The frequencies of these levels are arranged symmetrically around a central peak, for which the resonant spatial intensity pattern arises only from one half of the resonators. The central peak emits light only from one sublattice. This effect, known as sublattice polarization [99], exists also for midgap states in an undeformed graphene system, but then is confined to the edges of the device. We observed in Fig. 12 that these edge states transform continuously into the well isolated 0-th order pseudo-Landau level peak, which then emits from a wide area in the middle of the sample, thereby establishing a surprising direct connection of these two phenomena. The second signature of topology observed is a systematic connection between the wave intensity patterns of different Landau levels. A pattern on one sublattice in

Optical Materials EXPRESS

one level is identical to the pattern of the other sublattice in the next level. Mathematically, this effect is related to a deep fundamental phenomenon originating in particle physics, known as supersymmetry, which applies to the experimental setting because of the relativistic physics emerging near the Dirac points. As for the central level, we managed to confirm this effect by following the formation of pseudo-Landau levels in the complete transition from vanishing to large pseudo-magnetic field strengths [41], which was made possible by the flexible experimental setup.

These results connect features of a specific device to very general theoretical phenomena that can be applied to many other settings. Consequently, this work provides a framework to design a wide range of novel optical devices operating with unprecedented precision, and paves a way to generate flat bands – systems in which many states have the same energy or frequency – which can be used to enhance light-matter interactions with promising applications for solar cells or energy harvesting systems. Furthermore, it would be interesting to explore the utility of this setup as a sublattice-dependent sensor, where one would exploit that certain external fields can break the chiral symmetry in our system, for which no sensors presently exist.

8. Towards nonlinear systems

As already indicated in the introduction (see Fig. 1), we are able to locally integrate additional linear (see Section 7.1) and even nonlinear absorption into our system. Adding linear absorption is simply done by placing absorbing patches or spraying an absorptive graphite layer on top of the resonators and resonance widths of single resonators can be increased up to a factor 100 [37]. In order to add nonlinear absorption we use different diodes, that are embedded in metallic loops and couple them inductively by placing them over the resonators using Teflon spacers. The single resonator response with inductively coupled diode can be seen in Fig. 13(a). For small powers a decrease of the resonance height due to an increase of the resonance width is observed, whereas for higher powers an additional frequency shift is seen as well. The nonlinearity can be used in a wide range of systems and opens up path to interesting experiments, combining nonlinearity and topology.

One possible application of such a nonlinear topological system, is a self-shielded topological receiver protector (RP) [38,100]. RPs shield sensitive electronics from high-power incoming signals that might damage them and are widely used in (wireless) communication and radar setups [see Fig. 13(b)]. We implemented the topological RP using an SSH chain of 17 coupled resonators with central defect [see Fig. 13(d)]. The leftmost and rightmost resonators are coupled to kink antennas and we place a diode on top of the central resonator, where the defect-mode is (exponentially) localized [see Fig. 8(a) and (e)]. We then measured the transmission through the resonator array for increasing power P_{in}. Results are presented in Fig. 13(c). For small incident powers the transmission between the two antennas shows a high peak resonance associated with the topologically induced resonant-defect-mode (zero-mode). When we now increase the power, the nonlinear losses of the diode are activated. The resonant mode experiences a self-induced transition from an underdamping to an overdamping regime, destroying the resonant-defect mode. Since the resonance itself is vanishing, the peak in the transmittance is gradually suppressed and simultaneously the reflectance approaches 1 (not shown here, see Ref. [100] for details).

We may note here, that a single resonator with diode on top, coupled to two antennas is already an RP, but one with very limited dynamic range. High input signals will be absorbed directly by the diode, causing its overheating or even destruction. Its implementation inside a C-symmetric photonic circuit [35,101] on the topological defect creating a zero-mode for low powers which is destructed for high powers. Thus the scattering profile of the incident wave changes from an exponential increase to defect resonator on the sublattice to an exponential decrease. This behaviour give rise to a decrease of transmittance, an increase of reflectance without an increase

Optical Materials EXPRESS

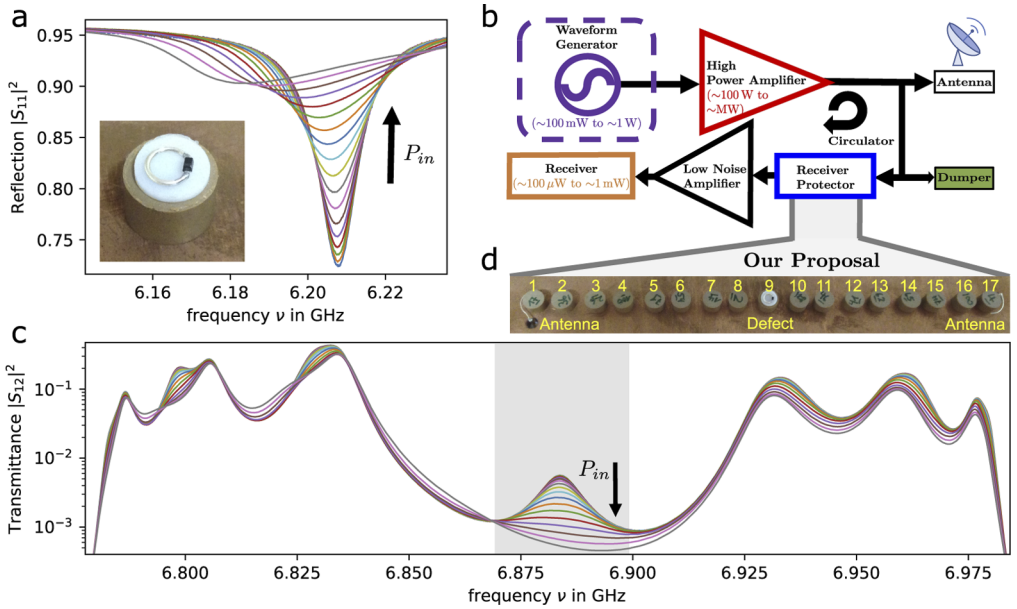

Fig. 13. (d) Proposed implementation of the RP consisting of 17 resonators with central defect. The incoming signal is injected via the left antenna with a power P_{in} and transmitted via the right antenna. The central resonator has a diode positioned on top of it using a Teflon spacer of 1 mm height [see photograph in (a)]. (b) Application of the RP in a radar setup. (a) Reflection spectra $|S_{11}|^2$ for an isolated resonator inductively coupled to a diode and (c) the transmittance spectra $|S_{21}|^2$ of the proposed RP for increasing input power P_{in} ranging from -30 (blue) to 4 dBm (grey) in steps of 2 dBm. The black arrow indicates the direction of increasing power. The reflection spectra were measured using a weakly coupled kink antenna. In (c) one can clearly see the two bands and the defect state in the middle of the band gap. The bulk-states within the two bands are hardly affected by the nonlinearity, while the central peak is vanishing for increasing power. The grey area is showing the frequency-range, where the RP is operating. Adapted from Ref. [100].

of absorbance (for details see [38,100]) for increasing power signals. Thus the RP survives significant greater input powers before it will be destroyed compared to a single resonator.

9. Conclusion

In the remarkably vivid domain of topological photonics, experiments performed in the microwave regime play a leading role. In this review we focused our attention to a specific platform consisting of evanescently coupled dielectric resonators excited by TE-polarized microwaves. The limited constraints in terms of fabrication allows to emulate lattices (with up to a few hundreds of sites) of any 1D or 2D geometries: periodic (with complex unit cell), uniformly or non-homogeneously deformed or disordered. Edges and defects can also be implemented at will. Moreover, intrinsic properties of each resonator can be individually tuned (e.g. resonant frequency, losses) and can be even equipped with a nonlinear response. The coupling between two resonators can be finely adjusted on demand over one order of magnitude. For a given lattice, both amplitude and phase of the reflected and/or transmitted signals are measured with a high degree of accuracy and large dynamics, allowing a precise extraction of the local density of states, and consequently of the density of states and their spatial distribution.

Optical Materials EXPRESS

With this versatile and flexible experimental platform we tackled several important topological photonic topics ranging from transport enhancement by means of a non $\mathcal{PT}$-symmetric interface state, to a new type of non sacrificial fuses based on self-shielded topological receiver protectors, but also from Dirac points merging to the continuous transformation of edge state into Landau level under the influence of a giant pseudo-magnetic field. We showed also that far from hindering topological effects, high-order couplings may be used to generate subtle symmetry breaking, promoting defect state with enhanced topological protection. This results illustrate that the microwave resonator lattices constitute an ideal photonic topological material for both fundamental studies and applications.

In the near future, we will take advantage of the multiple possibilities offered by this experimental platform to address exciting topics at the crossroads of topological physics, disorder and non-linearity.

Acknowledgments. We are deeply grateful to Gilles Montambaux, Henning Schomerus and Tsampikos Kottos for their fruitful and enlightening collaborations. We wish to thank Olivier Legrand for stimulating discussions and for a careful reading of the manuscript

Disclosures. The authors declare no conflicts of interest.

References

1. K. v. Klitzing, G. Dorda, and M. Pepper, "New method for high-accuracy determination of the fine-structure constant based on quantized Hall resistance," Phys. Rev. Lett. **45**(6), 494–497 (1980).
2. K. V. Klitzing, T. Chakraborty, P. Kim, V. Madhavan, X. Dai, J. McIver, Y. Tokura, L. Savary, D. Smirnova, A. M. Rey, C. Felser, J. Gooth, and X. Qi, "40 years of the quantum Hall effect," Nat. Rev. Phys. **2**(8), 397–401 (2020).
3. M. Z. Hasan and C. L. Kane, "Colloquium: Topological insulators," Rev. Mod. Phys. **82**(4), 3045–3067 (2010).
4. M. Franz and L. Molenkamp, *Topological insulators* (Elsevier, 2013).
5. J. K. Asbóth, L. Oroszlány, and A. Pályi, *A Short Course on Topological Insulators* (Springer International Publishing, 2016).
6. J. D. Joannopoulos, S. G. Johnson, J. N. Winn, and R. D. Meade, *Photonic Crystals: Molding the Flow of Light* (Princeton University Press, 2008).
7. F. D. M. Haldane and S. Raghu, "Possible realization of directional optical waveguides in photonic crystals with broken time-reversal symmetry," Phys. Rev. Lett. **100**(1), 013904 (2008).
8. Z. Wang, Y. Chong, J. D. Joannopoulos, and M. Soljačić, "Observation of unidirectional backscattering-immune topological electromagnetic states," Nature **461**(7265), 772–775 (2009).
9. M. C. Rechtsman, J. M. Zeuner, A. Tünnermann, S. Nolte, M. Segev, and A. Szameit, "Strain-induced pseudomagnetic field and photonic Landau levels in dielectric structures," Nat. Photonics **7**(2), 153–158 (2013).
10. M. Hafezi, S. Mittal, J. Fan, A. Migdall, and J. M. Taylor, "Imaging topological edge states in silicon photonics," Nat. Photonics **7**(12), 1001–1005 (2013).
11. T. Ozawa, H. M. Price, A. Amo, N. Goldman, M. Hafezi, L. Lu, M. C. Rechtsman, D. Schuster, J. Simon, O. Zilberberg, and I. Carusotto, "Topological photonics," Rev. Mod. Phys. **91**(1), 015006 (2019).
12. P. St-Jean, V. Goblot, E. Galopin, A. Lemaître, T. Ozawa, L. Legratiet, I. Sagnes, J. Bloch, and A. Amo, "Lasing in topological edge states of a one-dimensional lattice," Nat. Photonics **11**(10), 651–656 (2017).
13. M. A. Bandres, S. Wittek, G. Harari, M. Parto, J. Ren, M. Segev, D. N. Christodoulides, and M. Khajavikhan, "Topological insulator laser: Experiments," Science **359**(6381), eaar4005 (2018).
14. D. Leykam and Y. D. Chong, "Edge solitons in nonlinear photonic topological insulators," Phys. Rev. Lett. **117**(14), 143901 (2016).
15. S. Mukherjee and M. C. Rechtsman, "Observation of Floquet solitons in a topological bandgap," Science **368**(6493), 856–859 (2020).
16. L. J. Maczewsky, M. Heinrich, M. Kremer, S. K. Ivanov, M. Ehrhardt, F. Martinez, Y. V. Kartashov, V. V. Konotop, L. Torner, D. Bauer, and A. Szameit, "Nonlinearity-induced photonic topological insulator," Science **370**(6517), 701–704 (2020).
17. S. Bittner, B. Dietz, M. Miski-Oglu, P. Oria Iriarte, A. Richter, and F. Schäfer, "Observation of a Dirac point in microwave experiments with a photonic crystal modeling graphene," Phys. Rev. B **82**(1), 014301 (2010).
18. S. Bittner, B. Dietz, M. Miski-Oglu, and A. Richter, "Extremal transmission through a microwave photonic crystal and the observation of edge states in a rectangular Dirac billiard," Phys. Rev. B **85**(6), 064301 (2012).
19. H.-J. Stöckmann and J. Stein, ""Quantum" chaos in billiards studied by microwave absorption," Phys. Rev. Lett. **64**(19), 2215–2218 (1990).
20. E. Doron, U. Smilansky, and A. Frenkel, "Experimental demonstration of chaotic scattering of microwaves," Phys. Rev. Lett. **65**(25), 3072–3075 (1990).

Optical Materials EXPRESS

21. H. Alt, H.-D. Gräf, H. L. Harney, R. Hofferbert, H. Lengeler, C. Rangacharyulu, A. Richter, and P. Schardt, "Superconducting billiard cavities with chaotic dynamics: An experimental test of statistical measures," Phys. Rev. E **50**(1), R1–R4 (1994).
22. H.-J. Stöckmann, *Quantum Chaos - An Introduction* (University Press, Cambridge, 1999).
23. D. Laurent, O. Legrand, P. Sebbah, C. Vanneste, and F. Mortessagne, "Localized modes in a finite-size open disordered microwave cavity," Phys. Rev. Lett. **99**(25), 253902 (2007).
24. G. J. Aubry, L. S. Froufe-Pérez, U. Kuhl, O. Legrand, F. Scheffold, and F. Mortessagne, "Experimental tuning of transport regimes in hyperuniform disordered photonic materials," Phys. Rev. Lett. **125**(12), 127402 (2020).
25. S. Ma, B. Xiao, Y. Yu, K. Lai, G. Shvets, and S. M. Anlage, "Topologically protected photonic modes in composite quantum Hall/quantum spin Hall waveguides," Phys. Rev. B **100**(8), 085118 (2019).
26. G.-G. Liu, Y. Yang, X. Ren, H. Xue, X. Lin, Y.-H. Hu, H.-X. Sun, B. Peng, P. Zhou, Y. Chong, and B. Zhang, "Topological anderson insulator in disordered photonic crystals," Phys. Rev. Lett. **125**(13), 133603 (2020).
27. S. Ma and S. M. Anlage, "Microwave applications of photonic topological insulators," Appl. Phys. Lett. **116**(25), 250502 (2020).
28. M. Bellec, U. Kuhl, G. Montambaux, and F. Mortessagne, "Tight-binding couplings in microwave artificial graphene," Phys. Rev. B **88**(11), 115437 (2013).
29. U. Kuhl, S. Barkhofen, T. Tudorovskiy, H.-J. Stöckmann, T. Hossain, L. de Forges de Parny, and F. Mortessagne, "Dirac point and edge states in a microwave realization of tight-binding graphene-like structures," Phys. Rev. B **82**(9), 094308 (2010).
30. J. A. Franco-Villafa ne, E. Sadurní, S. Barkhofen, U. Kuhl, F. Mortessagne, and T. H. Seligman, "First experimental realization of the Dirac oscillator," Phys. Rev. Lett. **111**(17), 170405 (2013).
31. T. Stegmann, J. A. Franco-Villafañe, Y. P. Ortiz, U. Kuhl, F. Mortessagne, and T. H. Seligman, "Microwave emulations and tight-binding calculations of transport in polyacetylene," Phys. Lett. A **381**(1), 24–29 (2017).
32. T. Stegmann, J. A. Franco-Villafa ne, U. Kuhl, F. Mortessagne, and T. H. Seligman, "Transport gap engineering by contact geometry in graphene nanoribbons: Experimental and theoretical studies on artificial materials," Phys. Rev. B **95**(3), 035413 (2017).
33. J. Böhm, M. Bellec, F. Mortessagne, U. Kuhl, S. Barkhofen, S. Gehler, H.-J. Stöckmann, I. Foulger, S. Gnutzmann, and G. Tanner, "Microwave experiments simulating quantum search and directed transport in artificial graphene," Phys. Rev. Lett. **114**(11), 110501 (2015).
34. P. Vignolo, M. Bellec, J. Böhm, A. Camara, J.-M. Gambaudo, U. Kuhl, and F. Mortessagne, "Energy landscape in a Penrose tiling," Phys. Rev. B **93**(7), 075141 (2016).
35. C. Poli, M. Bellec, U. Kuhl, F. Mortessagne, and H. Schomerus, "Selective enhancement of topologically induced interface states in a dielectric resonator chain," Nat. Commun. **6**(1), 6710 (2015).
36. C. Poli, M. Bellec, U. Kuhl, F. Mortessagne, and H. Schomerus, "Partial chiral symmetry-breaking as a route to spectrally isolated topological defect states in twodimensional artificial materials," 2D Mater. **4**(2), 025008 (2017).
37. M. Reisner, F. Mortessagne, E. Makri, T. Kottos, and U. Kuhl, "Microwave limiters implemented by coupled dielectric resonators based on a topological defect mode and CT-symmetry breaking," Acta Phys. Pol. A **136**(5), 790–796 (2019).
38. D. H. Jeon, M. Reisner, F. Mortessagne, T. Kottos, and U. Kuhl, "Non-Hermitian $\mathcal{CT}$-symmetric spectral protection of nonlinear defect modes," Phys. Rev. Lett. **125**(11), 113901 (2020).
39. M. Bellec, U. Kuhl, G. Montambaux, and F. Mortessagne, "Topological transition of Dirac points in a microwave experiment," Phys. Rev. Lett. **110**(3), 033902 (2013).
40. M. Bellec, U. Kuhl, G. Montambaux, and F. Mortessagne, "Manipulation of edge states in microwave artificial graphene," New J. Phys. **16**(11), 113023 (2014).
41. M. Bellec, C. Poli, U. Kuhl, F. Mortessagne, and H. Schomerus, "Observation of supersymmetric pseudo-Landau levels in strained microwave graphene," Light: Sci. Appl. **9**(1), 146 (2020).
42. D. Laurent, O. Legrand, P. Sebbah, C. Vanneste, and F. Mortessagne, "Localized modes in a finite-size open disordered microwave cavity," Phys. Rev. Lett. **99**(25), 253902 (2007).
43. E. Lidorikis, M. M. Sigalas, E. N. Economou, and C. M. Soukoulis, "Tight-binding parametrization for photonic band gap materials," Phys. Rev. Lett. **81**(7), 1405–1408 (1998).
44. U. Kuhl, S. Barkhofen, T. Tudorovskiy, H.-J. Stöckmann, T. Hossain, L. de Forges de Parny, and F. Mortessagne, "Dirac point and edge states in a microwave realization of tight-binding graphene-like structures," Phys. Rev. B **82**(9), 094308 (2010).
45. S. Barkhofen, M. Bellec, U. Kuhl, and F. Mortessagne, "Disordered graphene and boron nitride in a microwave tight-binding analog," Phys. Rev. B **87**(3), 035101 (2013).
46. J. Barthélemy, O. Legrand, and F. Mortessagne, "Complete *S*-matrix in a microwave cavity at room temperature," Phys. Rev. E **71**(1), 016205 (2005).
47. I. Rotter, "A non-Hermitian Hamilton operator and the physics of open quantum systems," J. Phys. A: Math. Theor. **42**(15), 153001 (2009).
48. U. Kuhl, O. Legrand, and F. Mortessagne, "Microwave experiments using open chaotic cavities in the realm of the effective Hamiltonian formalism," Fortschr. Phys. **61**(2-3), 404–419 (2013).
49. T. Tudorovskiy, R. Höhmann, U. Kuhl, and H. Stöckmann, "On the theory of cavities with point-like perturbations: part i. general theory," J. Phys. A: Math. Theor. **41**(27), 275101 (2008).

Optical Materials EXPRESS

50. M. Milićević, T. Ozawa, G. Montambaux, I. Carusotto, E. Galopin, A. Lemaître, L. L. Gratiet, I. Sagnes, J. Bloch, and A. Amo, "Orbital edge states in a photonic honeycomb lattice," Phys. Rev. Lett. **118**(10), 107403 (2017).
51. W. Su, J. Schrieffer, and A. Heeger, "Solitons in polyacetylene," Phys. Rev. Lett. **42**(25), 1698–1701 (1979).
52. S. K. Özdemir, S. Rotter, F. Nori, and L. Yang, "Parity–time symmetry and exceptional points in photonics," Nat. Mater. **18**(8), 783–798 (2019).
53. M. Parto, Y. G. N. Liu, B. Bahari, M. Khajavikhan, and D. N. Christodoulides, "Non-Hermitian and topological photonics: optics at an exceptional point," Nanophotonics **10**(1), 403–423 (2020).
54. M. A. Bandres and M. Segev, "Viewpoint: Non-Hermitian topological systems," Physics **11**, 96 (2018).
55. B. Midya, H. Zhao, and L. Feng, "Non-Hermitian photonics promises exceptional topology of light," Nat. Commun. **9**(1), 2674 (2018).
56. L. Feng, R. El-Ganainy, and L. Ge, "Non-Hermitian photonics based on parity–time symmetry," Nat. Photonics **11**(12), 752–762 (2017).
57. J. Zak, "Berry's phase for energy bands in solids," Phys. Rev. Lett. **62**(23), 2747–2750 (1989).
58. M. I. Katsnelson, *The Physics of Graphene* (Cambridge University Press, 2020), 2nd ed.
59. H. Aoki and M. S. Dresselhaus, *Physics of Graphene* (Springer International Publishing, 2014), 1st ed.
60. B. Duplantier, V. Rivasseau, and J. Nöel Fuchs, *Dirac Matter* (Birkhäuser, 2017), 1st ed.
61. J. Cayssol, "Introduction to Dirac materials and topological insulators," C. R. Phys. **14**(9-10), 760–778 (2013).
62. A. H. Castro Neto, F. Guinea, N. M. R. Peres, K. S. Novoselov, and A. K. Geim, "The electronic properties of graphene," Rev. Mod. Phys. **81**(1), 109–162 (2009).
63. G. Montambaux, "Artificial graphenes: Dirac matter beyond condensed matter," C. R. Phys. **19**(5), 285–305 (2018).
64. M. Polini, F. Guinea, M. Lewenstein, H. C. Manoharan, and V. Pellegrini, "Artificial honeycomb lattices for electrons, atoms and photons," Nat. Nanotechnol. **8**(9), 625–633 (2013).
65. L. M. Nash, D. Kleckner, A. Read, V. Vitelli, A. M. Turner, and W. T. M. Irvine, "Topological mechanics of gyroscopic metamaterials," Proc. Natl. Acad. Sci. **112**(47), 14495–14500 (2015).
66. D. Torrent and J. Sánchez-Dehesa, "Acoustic analogue of graphene: Observation of Dirac cones in acoustic surface waves," Phys. Rev. Lett. **108**(17), 174301 (2012).
67. C. He, X. Ni, H. Ge, X.-C. Sun, Y.-B. Chen, M.-H. Lu, X.-P. Liu, and Y.-F. Chen, "Acoustic topological insulator and robust one-way sound transport," Nat. Phys. **12**(12), 1124–1129 (2016).
68. S. Yves, F. Lemoult, M. Fink, and G. Lerosey, "Crystalline soda can metamaterial exhibiting graphene-like dispersion at subwavelength scale," Sci. Rep. **7**(1), 15359 (2017).
69. H. Zhu, T.-W. Liu, and F. Semperlotti, "Design and experimental observation of valley-Hall edge states in diatomic-graphene-like elastic waveguides," Phys. Rev. B **97**(17), 174301 (2018).
70. G. Montambaux, F. Piéchon, J.-N. Fuchs, and M. O. Goerbig, "Merging of Dirac points in a two-dimensional crystal," Phys. Rev. B **80**(15), 153412 (2009).
71. G. Montambaux, F. Piéchon, J. Fuchs, and M. O. Goerbig, "A universal Hamiltonian for motion and merging of Dirac points in a two-dimensional crystal," Eur. Phys. J. B **72**(4), 509–520 (2009).
72. K. Nakada, M. Fujita, G. Dresselhaus, and M. Dresselhaus, "Edge state in graphene ribbons: Nanometer size effect and edge shape dependence," Phys. Rev. B **54**(24), 17954–17961 (1996).
73. L. Brey and H. A. Fertig, "Electronic states of graphene nanoribbons studied with the Dirac equation," Phys. Rev. B **73**(23), 235411 (2006).
74. M. Kohmoto and Y. Hasegawa, "Zero modes and edge states of the honeycomb lattice," Phys. Rev. B **76**(20), 205402 (2007).
75. Y. Kobayashi, K. Fukui, T. Enoki, K. Kusakabe, and Y. Kaburagi, "Observation of zigzag and armchair edges of graphite using scanning tunneling microscopy and spectroscopy," Phys. Rev. B **71**(19), 193406 (2005).
76. Y. Niimi, T. Matsui, H. Kambara, K. Tagami, M. Tsukada, and H. Fukuyama, "Scanning tunneling microscopy and spectroscopy of the electronic local density of states of graphite surfaces near monoatomic step edges," Phys. Rev. B **73**(8), 085421 (2006).
77. S. Ryu and Y. Hatsugai, "Topological origin of zero-energy edge states in particle-hole symmetric systems," Phys. Rev. Lett. **89**(7), 077002 (2002).
78. P. Delplace, D. Ullmo, and G. Montambaux, "Zak phase and the existence of edge states in graphene," Phys. Rev. B **84**(19), 195452 (2011).
79. M. C. Rechtsman, Y. Plotnik, J. M. Zeuner, D. Song, Z. Chen, A. Szameit, and M. Segev, "Topological creation and destruction of edge states in photonic graphene," Phys. Rev. Lett. **111**(10), 103901 (2013).
80. M. Atala, M. Aidelsburger, J. Barreiro, D. Abanin, T. Kitagawa, E. Demler, and I. Bloch, "Direct measurement of the zak phase in topological bloch bands," Nat. Phys. **9**(12), 795–800 (2013).
81. C. Poli, H. Schomerus, M. Bellec, U. Kuhl, and F. Mortessagne, "Partial chiral symmetry-breaking as a route to spectrally isolated topological defect states in two-dimensional artificial materials," 2D Mater. **4**(2), 025008 (2017).
82. L. Lu, J. D. Joannopoulos, and M. Soljačić, "Topological photonics," Nat. Photonics **8**(11), 821–829 (2014).
83. C.-K. Chiu, J. C. Y. Teo, A. P. Schnyder, and S. Ryu, "Classification of topological quantum matter with symmetries," Rev. Mod. Phys. **88**(3), 035005 (2016).
84. B. Sutherland, "Localization of electronic wave functions due to local topology," Phys. Rev. B **34**(8), 5208–5211 (1986).
85. E. H. Lieb, "Two theorems on the Hubbard model," Phys. Rev. Lett. **62**(10), 1201–1204 (1989).

Optical Materials EXPRESS

86. J. C. Y. Teo and C. L. Kane, "Topological defects and gapless modes in insulators and superconductors," Phys. Rev. B **82**(11), 115120 (2010).
87. L. Tang, D. Song, S. Xia, S. Xia, J. Ma, W. Yan, Y. Hu, J. Xu, D. Leykam, and Z. Chen, "Photonic flat-band lattices and unconventional light localization," Nanophotonics **9**(5), 1161–1176 (2020).
88. S. Xia, A. Ramachandran, S. Xia, D. Li, X. Liu, L. Tang, Y. Hu, D. Song, J. Xu, D. Leykam, S. Flach, and Z. Chen, "Unconventional flatband line states in photonic Lieb lattices," Phys. Rev. Lett. **121**(26), 263902 (2018).
89. R. A. Vicencio, C. Cantillano, L. Morales-Inostroza, B. Real, C. Mejía-Cortés, S. Weimann, A. Szameit, and M. I. Molina, "Observation of localized states in Lieb photonic lattices," Phys. Rev. Lett. **114**(24), 245503 (2015).
90. S. Mukherjee, A. Spracklen, D. Choudhury, N. Goldman, P. Öhberg, E. Andersson, and R. R. Thomson, "Observation of a localized flat-band state in a photonic Lieb lattice," Phys. Rev. Lett. **114**(24), 245504 (2015).
91. M. O. Goerbig, "Quantum Hall effects," (2009). ArXiv:0909.1998.
92. S. M. Girvin, *Topological Aspects of Low-Dimensional Systems–École d'Été de Physique Théorique LXIX* (Springer, 1999), chap., "The Quantum Hall Effect: Novel Excitations and Broken Symmetries, " ArXiv:cond-mat/9907002.
93. G. L. J. A. Rikken and B. A. van Tiggelen, "Observation of magnetically induced transverse diffusion of light," Nature **381**(6577), 54–55 (1996).
94. F. Guinea, M. I. Katsnelson, and A. K. Geim, "Energy gaps and a zero-field quantum Hall effect in graphene by strain engineering," Nat. Phys. **6**(1), 30–33 (2010).
95. N. Levy, S. A. Burke, K. L. Meaker, M. Panlasigui, A. Zettl, F. Guinea, A. H. C. Neto, and M. F. Crommie, "Strain-induced pseudo–magnetic fields greater than 300 tesla in graphene nanobubbles," Science **329**(5991), 544–547 (2010).
96. H. Abbaszadeh, A. Souslov, J. Paulose, H. Schomerus, and V. Vitelli, "Sonic Landau levels and synthetic gauge fields in mechanical metamaterials," Phys. Rev. Lett. **119**(19), 195502 (2017).
97. X. Wen, C. Qiu, Y. Qi, L. Ye, M. Ke, F. Zhang, and Z. Liu, "Acoustic Landau quantization and quantum-Hall-like edge states," Nat. Phys. **15**(4), 352–356 (2019).
98. O. Jamadi, E. Rozas, G. Salerno, M. Milićević, T. Ozawa, I. Sagnes, A. Lemaître, L. L. Gratiet, A. Harouri, I. Carusotto, J. Bloch, and A. Amo, "Direct observation of photonic Landau levels and helical edge states in strained honeycomb lattices," Light: Sci. Appl. **9**(1), 144 (2020).
99. C. Poli, J. Arkinstall, and H. Schomerus, "Degeneracy doubling and sublattice polarization in strain-induced pseudo-Landau levels," Phys. Rev. B **90**(15), 155418 (2014).
100. M. Reisner, D. H. Jeon, C. Schindler, H. Schomerus, F. Mortessagne, U. Kuhl, and T. Kottos, "Self-shielded topological receiver protectors," Phys. Rev. Appl. **13**(3), 034067 (2020).
101. H. Schomerus, "Topologically protected midgap states in complex photonic lattices," Opt. Lett. **38**(11), 1912–1914 (2013).